

8-1-2024

# Thermodynamic Feasibility of Potential Nano-Energetic Systems Based on Metal Oxynitrides

Manoj Chhetri  
*The University of Texas Rio Grande Valley*

Follow this and additional works at: <https://scholarworks.utrgv.edu/etd>



Part of the [Physics Commons](#)

---

## Recommended Citation

Chhetri, Manoj, "Thermodynamic Feasibility of Potential Nano-Energetic Systems Based on Metal Oxynitrides" (2024). *Theses and Dissertations*. 1609.  
<https://scholarworks.utrgv.edu/etd/1609>

This Thesis is brought to you for free and open access by ScholarWorks @ UTRGV. It has been accepted for inclusion in Theses and Dissertations by an authorized administrator of ScholarWorks @ UTRGV. For more information, please contact [justin.white@utrgv.edu](mailto:justin.white@utrgv.edu), [william.flores01@utrgv.edu](mailto:william.flores01@utrgv.edu).

THERMODYNAMIC FEASIBILITY OF POTENTIAL NANO-ENERGETIC  
SYSTEMS BASED ON METAL OXYNITRIDES

A Thesis

by

MANOJ CHHETRI

Submitted in Partial Fulfillment of the  
Requirements for the Degree of  
MASTER OF SCIENCE

Major Subject: Interdisciplinary Studies

The University of Texas Rio Grande Valley  
August 2024



THERMODYNAMIC FEASIBILITY OF POTENTIAL NANO-ENERGETIC  
SYSTEMS BASED ON METAL OXYNITRIDES

A Thesis  
by  
MANOJ CHHETRI

COMMITTEE MEMBERS

Dr. Karen S. Martirosyan  
Chair of Committee

Dr. Mircea Chipara  
Committee Member

Dr. Ahmed Touhami  
Committee Member

Dr. Soma Mukherjee  
Committee Member

August 2024



Copyright 2024 Manoj Chhetri

All Rights Reserved



## ABSTRACT

Chhetri, Manoj, Thermodynamic Feasibility of Potential Nano-energetic Systems based on Metal Oxynitrides. Master of Science (MS), August 2024, 63 pp., 2 tables, 22 figures, 59 references.

A computational study was undertaken with the objective of identifying the nano-energetic systems containing aluminum as fuel and metal oxynitrides as oxidizer, aiming to achieve an exothermic reaction characterized by the maximum values of gas generation, adiabatic combustion temperature, and energy release. For the thermodynamic calculation, nine systems based on metal oxynitrides were taken using the THERMO software that works based on the Gibbs free energy minimization, together with HSC Chemistry 7 to calculate the thermodynamic equilibrium concentrations of reactants and products corresponding gas generation, temperature and energy release by varying the fuel to oxidizer ratio. Among all the chosen oxynitride systems, the bismuth oxynitrate hydrate ( $\text{BiONO}_3 \cdot \text{H}_2\text{O}$ ) showed the maximum value of combustion temperature of above 3600 K for 23.12 wt.% of aluminum fuel along with energy release rate of -9.730 kJ/cc, and a maximum value of gas discharge, 3.004 L/g. With the favorable stoichiometry of reactants, the combustion temperature, and the volume of gas generation of  $\text{BiONO}_3 \cdot \text{H}_2\text{O}$  was followed by the perovskite type of oxynitrides with adiabatic combustion temperature values more than 3000K. Titanium nickel oxynitride ( $\text{TiNiON}$ ) showed fascinating result with maximum energy release among all the systems taken with the value of -10.699 kJ/cc and a notably high temperature of 2413 K but is completely lacking a gas discharge. In addition, the electronic structure and optical behaviors of the oxynitrides were analyzed based on ab-initio density functional theory (DFT) in order to explain the energetic behavior as well as their photothermal conversion and possible reaction ignition by the light sources.



## DEDICATION

This thesis is dedicated to the three most important people in my life, who have been unwavering pillars of support, inspiration, and love. To my beloved wife, Nisha Basnet Chhetri, whose boundless encouragement, patience, and understanding have been my source of strength throughout this journey. Your unwavering belief in me has propelled me forward, and I am forever grateful for your presence in my life. To my son, Kritik Chhetri, whose innocent joy, and endless curiosity remind me of the greater purpose behind my academic pursuits. Your laughter has been my motivation, and I dedicate this work to shaping a better future for you and generations to come and to my late father, Surya Bahadur Chhetri, whose support, and sacrifices have laid the foundation for my aspirations and achievements.



## ACKNOWLEDGMENTS

I extend my sincerest gratitude to my research advisor, Prof. Dr. Karen Martirosyan, for his invaluable guidance and unwavering support throughout this research endeavor. His expertise and mentorship have been instrumental in shaping the direction and quality of this work. I am deeply appreciative of Dr. Mkhitar Hobosyan for his generous assistance and insightful feedback, which have significantly contributed to the refinement of this thesis. I am indebted to my esteemed thesis committee members, Dr. Soma Mukherjee, Dr. Ahmed Touhami, and Dr. Mircea Chipara, for their expertise, constructive criticism, and dedication to ensuring the scholarly rigor of this study.



## TABLE OF CONTENTS

	Page
ABSTRACT .....	iii
DEDICATION .....	iv
ACKNOWLEDGMENTS .....	v
LIST OF TABLES .....	viii
LIST OF FIGURES .....	ix
CHAPTER I: INTRODUCTION .....	1
1.1 Energetic Materials .....	1
1.2 Nano-energetic Materials .....	3
1.3 Thermodynamics and Nano-energetics .....	4
CHAPTER II: ANALYSIS OF CURRENT TRENDS .....	6
CHAPTER III: SYSTEMS UNDER STUDY .....	12
3.1 Perovskite Type of Oxynitrides, $ABO_2N$ (A=Ba, Sr, Ca and B=Ta, Nb) .....	12
3.2 Bismuth Oxynitrate Hydrate ( $BiONO_3 \cdot H_2O$ ) .....	16
3.3 Potassium Germanium Oxynitride (KGeON) .....	16
3.4 Sodium Silicon Oxynitride (NaSiON) .....	17
3.5 Titanium Nickel Oxynitride (TiNiON) .....	18
CHAPTER IV: METHODOLOGY .....	20
4.1 Thermodynamic Calculations .....	20
4.2 Overview of Density Functional Theory (DFT) .....	23
4.2.1 Forms of the Schrödinger Equation: .....	23
4.2.2 Theoretical Foundations of DFT .....	24
CHAPTER V: RESULTS AND DISCUSSIONS .....	28
5.1 Chemical Reactions and Thermodynamic Analysis .....	28
5.1.1 Equilibrium Concentration of Products and Adiabatic Combustion Temperature .....	28
5.1.2 Volumetric and Gravimetric Energy Release out of the Exothermic Reactions .....	38

5.1.3	Reactions Involved of Favorable Reactant's Stoichiometry . . . . .	39
5.1.4	Amount of Gas Release out of the Exothermic Reaction of Reactant Mix- tures . . . . .	41
5.2	Density Functional Theory (DFT) Analysis . . . . .	44
5.2.1	Electronic Band Structure and Density of States (DOS) . . . . .	44
5.2.2	Optical Properties Calculations . . . . .	48
CHAPTER VI: CONCLUSIONS . . . . .		54
REFERENCES . . . . .		58
VITA . . . . .		63

## LIST OF TABLES

	Page
Table 5.1: Thermite reactants and their corresponding gas species. . . . .	43
Table 5.2: Maximum adiabatic combustion temperature, gas generation and energy release for several oxidizer compounds. . . . .	44



## LIST OF FIGURES

	Page
Figure 1.1: Energetic materials broadly categorized as explosives, propellants and pyrotechnics. . . . .	1
Figure 2.1: Energy densities of some monomolecular energetic materials (TNT, RDX, PETN) and some thermite composites [14]. . . . .	7
Figure 3.1: Molecular structure of perovskite metal oxynitrides of the form $ABO_2N$ . . . . .	13
Figure 3.2: Molecular crystal structure of potassium germanium oxynitrides ( $KGeON$ ). . . . .	17
Figure 3.3: Molecular structure of sodium silicon oxynitrides ( $NaSiON$ ). . . . .	18
Figure 5.1: Adiabatic combustion temperature and equilibrium concentration of reaction products by varying the fuel to oxidizer ratio for $Al/BiONO_3 \cdot H_2O$ system. . . . .	29
Figure 5.2: Adiabatic combustion temperature and equilibrium concentration of reaction products by varying the fuel to oxidizer ratio for $Al/CaTaO_2N$ system. . . . .	30
Figure 5.3: Adiabatic combustion temperature and equilibrium concentration of reaction products by varying the fuel to oxidizer ratio for $Al/CaNbO_2N$ system. . . . .	31
Figure 5.4: Adiabatic combustion temperature and equilibrium concentration of reaction products by varying the fuel to oxidizer ratio for $Al/SrNbO_2N$ system. . . . .	32
Figure 5.5: Adiabatic combustion temperature and equilibrium concentration of reaction products by varying the fuel to oxidizer ratio for $Al/SrTaO_2N$ system. . . . .	33
Figure 5.6: Adiabatic combustion temperature and equilibrium concentration of reaction products by varying the fuel to oxidizer ratio for $Al/BaTaO_2N$ . . . . .	34
Figure 5.7: Adiabatic combustion temperature and equilibrium concentration of reaction products by varying the fuel to oxidizer ratio for $Al/TiNiON$ system. . . . .	35
Figure 5.8: Adiabatic combustion temperature and equilibrium concentration of reaction products by varying the fuel to oxidizer ratio for $Al/KGeON$ system. . . . .	36
Figure 5.9: adiabatic combustion temperature and equilibrium concentration of reaction products by varying the fuel to oxidizer ratio for $Al/NaSiON$ system. . . . .	37
Figure 5.10: Volumetric and gravimetric energy release for the most favorable stoichiometry of Al-oxynitride formulation. . . . .	38
Figure 5.11: Variation of gas generation for different metal oxynitride formulations by varying fuel to oxidizer ratio. . . . .	42
Figure 5.12: Electronic band structure and density of states of $CaTaO_2N$ . . . . .	46
Figure 5.13: Electronic band structure and density of states of $KGeON$ . . . . .	47

Figure 5.14: Electronic band structure and density of states of NaSiON. . . . .	48
Figure 5.15: Optical properties of CaTaO <sub>2</sub> N. . . . .	51
Figure 5.16: Optical properties of KGeON. . . . .	52
Figure 5.17: Optical properties of NaSiON. . . . .	53

## CHAPTER I

### INTRODUCTION

#### 1.1 Energetic Materials

Energetic materials (EMs) are a diverse class of substances known for their ability to release energy upon detonation in a controlled manner and have played a vital role in various technological and military applications throughout history. The term "energetic materials" encompasses a wide range of substances, including explosives, propellants, and pyrotechnics, all of which are characterized by their capacity to undergo exothermic reactions, resulting in the release of large amounts of stored chemical energy into other forms of energy. The history of energetic materials dates back centuries, with the earliest documented use of gunpowder in ancient China during the 9th century [1]. Chinese alchemists accidentally discovered the explosive properties of a mixture containing saltpeter (potassium nitrate), charcoal, and sulfur, laying the strong foundation for the development of early explosive devices and firearms [2].

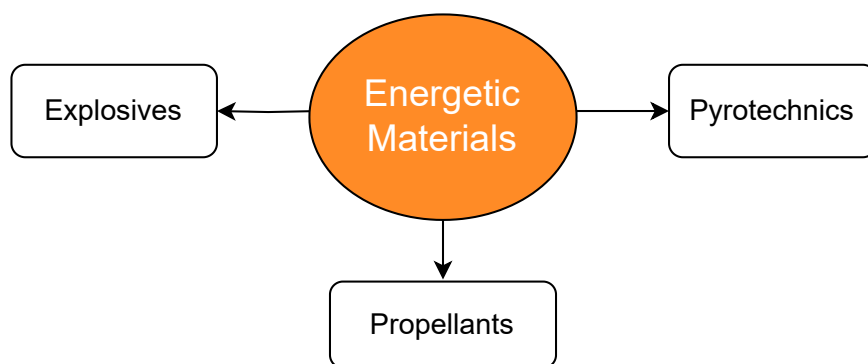


Figure 1.1: Energetic materials broadly categorized as explosives, propellants and pyrotechnics.

This invention significantly influenced military tactics and warfare dynamics. Over the following centuries, the understanding and application of energetic materials evolved across different cultures and regions. The spread of gunpowder technology reached the Middle East and Europe, leading to further advancements in weaponry and the emergence of pyrotechnic displays for celebratory purposes. The 19th and 20th centuries witnessed a rapid expansion of knowledge and scientific research in the field of energetic materials [3].

The use of energetic materials has grown fast with wide range of applications. Innovations such as nitrocellulose-based propellants and dynamite revolutionized industrial processes, mining, and construction. Military applications continued to drive advancements in explosive technologies, culminating in the development of powerful high explosives during World War I and World War II [4]. In addition to military and defense, the aerospace industry heavily relies on energetic materials for rocket propulsion, powering launch vehicles, satellites, and spacecraft into orbit. Additionally, these materials are essential in pyrotechnic devices for aerospace functions such as stage separation and airbag deployment, ensuring the success and safety of space missions. In the fields of mining and construction, energetic materials, particularly explosives, play a vital role in controlled blasting. These materials are crucial for extracting minerals, reshaping landscapes, and facilitating efficient and safe excavation processes in various industrial applications. Also, such materials have application in the oil and gas industry using perforating charges. These charges, containing energetic components, create perforations in well casings to enhance oil and gas extraction, demonstrating their importance in energy resource development. Specially, the pyrotechnics contribute to entertainment industries such as fireworks and special effects in film. In fireworks displays, pyrotechnic compositions, often containing energetic materials, create dazzling visual spectacles. Similarly, these materials enhance the realism of explosions and visual effects in the film and entertainment sector. Energetic materials play a critical role in automotive safety through their use in airbag inflators. Rapid gas generation from these materials during a collision ensures the swift deployment of airbags, protecting vehicle occupants and illustrating their importance in vehicular safety systems. For such a system the energetic materials

should be chosen to be the one which has the potential to generate extreme gas discharge in a matter of milliseconds. Furthermore, such materials also have their applications in research and medical fields. They are essential in research settings for studying shockwaves, detonation mechanisms, and combustion processes such as in shock tubes and detonation studies, enabling scientists to explore fundamental aspects of energetic reactions and their effects on materials. They also contribute to medical applications through their use in pharmaceutical propellants for inhalers [5]. The controlled release of medication facilitated by these materials aids in the effective delivery of therapeutic agents to patients, showcasing their versatility beyond traditional explosive applications.

## **1.2 Nano-energetic Materials**

In recent decades, the study and development of energetic materials have expanded beyond traditional applications. The field now encompasses research into more sophisticated and advanced energetic system in the name of nano energetic materials (NMs) or nano-thermites, also refer to as metastable intermolecular composites (MICs) [6, 7]. Nano-energetics involve the mixture of fuel and oxidizer particles with the manipulation of materials at the nanoscale to enhance their performance, reactivity, and safety [8–10]. Modern research aims to not only improve the energy density and efficiency of energetic materials but also for their stability to address environmental and safety concerns associated with their use [11–13]. The design and synthesis of novel materials, including metal oxynitrides, represent a frontier in the quest for next-generation energetic systems with enhanced performance and reduced environmental impact. As the exploration of nanotechnology and advanced materials continues, the historical trajectory of energetic materials converges with cutting-edge scientific and technological innovations, offering new possibilities for energy storage, propulsion, and other applications. The intersection of nanotechnology and energetic materials opens avenues for research into materials with tailored properties, setting the stage for a transformative impact on various industries and technologies [14]. In the pursuit of sustainable and efficient energy solutions, the exploration of innovative materials and systems has become imperative. Nanotechnology, with its ability to manipulate matter at the nanoscale,

opens large space for the development of novel nano-energetic materials and systems that hold great promise for diverse applications. Metal oxynitrides, a class of compounds encompassing both metal oxides and nitrides, emerge as intriguing candidates for advancing the frontiers of nano-energetics.

### **1.3 Thermodynamics and Nano-energetics**

Thermodynamics, one of the fundamental branches of physical science, that deals with the relations between heat flow and all other forms of energy, plays a crucial role in understanding the energetics and stability of materials, thereby guiding the design and optimization of energy storage and release processes [15]. Thermodynamics of the material describes about several energetics and thermal properties of materials considering the energy and thermal behaviors. At the nanoscale, where materials exhibit unique and often unconventional behaviors, the principles of thermodynamics provide a critical lens through which we can comprehend the energetic landscapes of these intricate systems. The study of thermodynamics not only facilitates a complete understanding of the energy transformations within nanostructures but also serves as a foundational framework to predict, analyze, and enhance the performance of nano-energetic systems by elucidating the thermodynamic feasibility, stability, and efficiency of energy storage and release processes. The intersection of thermodynamics and nanotechnology provides the path to assess the feasibility and performance of potential nano-energetic systems [16].

This thesis embarks on a comprehensive exploration of the thermodynamic feasibility of potential nano-energetic systems centered around metal oxynitrides. By delving into the thermodynamic principles governing these systems, we aim to elucidate the intricate relationships between structure, composition, and energetic performance. The computational examination of metal oxynitride nanostructures will be crucial, enabling a detailed analysis of their thermodynamic properties and offering insights into the potential applications in energy storage, propulsion, and other technological domains. Furthermore, this study endeavors to contribute to the broader discourse on sustainable energy by evaluating the environmental impact and safety considerations associated with metal oxynitride-based nano-energetic systems. Understanding the

thermodynamics of these materials is paramount not only for their technological implications but also for ensuring their responsible and ethical integration into our energy landscape.

As we go on this exploration, the integration of theoretical models and computational simulations will provide a multidimensional perspective, offering a nuanced understanding of the thermodynamics of metal oxynitride-based nano-energetic systems. Through this interdisciplinary approach, we aspire to pave the way for the development of efficient and environmentally conscious energy solutions, contributing to the ongoing global efforts towards a sustainable and resilient future.

## CHAPTER II

### ANALYSIS OF CURRENT TRENDS

The energetic materials when ignited externally undergoes highly exothermic reaction producing a high amount of energy, thermal pulse, and gas generation [17]. Traditional energetic materials include a single monomolecular compound formed by repetition of similar structures while the nano-thermites include composite formulation of suitable fuel and oxidizer at nano scale with high energy density and fast reaction rates [18]. They can generate large amounts of gaseous products, which makes them useful alternatives for explosives and propellants, and are easily tunable for specific applications such as micro-thrusters for space exploration [19]. Nano thermites are typically composed of a metal fuel as reducing agent, and oxidizers in the form of oxides [10, 20, 21]. Recently Martirosyan's group proposed also to use hydroxides as reducing agent [16, 22]. At least one of the reagents is in nanosized domain [23], which ensures high surface area-to-volume ratio, leading to a faster reaction rates and more complete combustion in short span of time, which cannot be achieved with larger particle size constituents. The oxidizer helps to facilitate the combustion by providing oxygen or other oxidizing agents to help sustain the exothermic reaction. Several computational and experimental studies have been done so far to understand and explore the possibilities of such nanocomposites to understand the chemical energy associated, the amount of energy release during combustion, the adiabatic combustion temperature generation, and ways of controlling the energy and gas pressure discharge [24].

Figure 2.1 shows the energy densities per volume and mass for most popular monomolecular energetic materials (TNT, RDX, PETN) and thermite composites [14]. Traditional energetic materials include mono-molecular compounds like 2,4,6-trinitrotoluene (TNT), 1,3,5-trinitroperhydro-1,3,5-triazine (RDX), pentaerythritol tetranitrate (PETN) etc. which can generate the volumet-

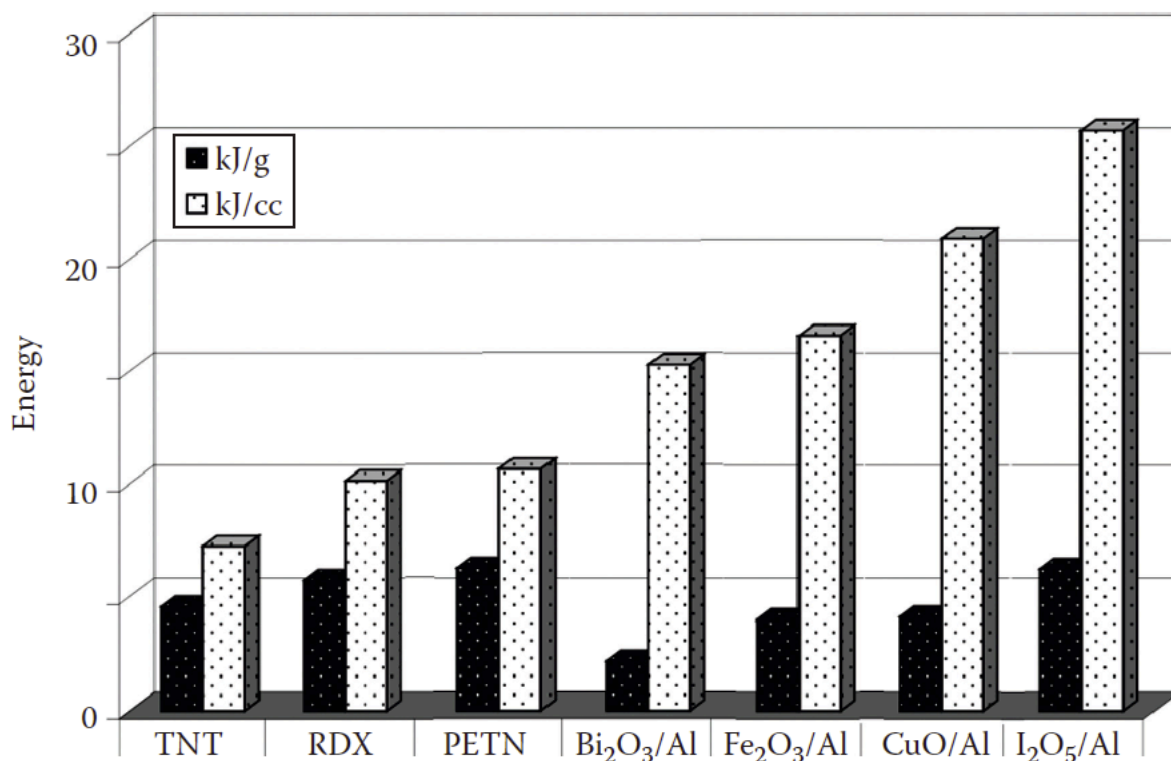


Figure 2.1: Energy densities of some monomolecular energetic materials (TNT, RDX, PETN) and some thermite composites [14].

ric energy of  $\approx 7.5$  kJ/cc for TNT and  $\approx 10$  kJ/cc for RDX, and PETN respectively [10, 24, 25]. But the newly and widely studied nanocomposites of aluminum as metal fuel and metal oxides such as CuO, Fe<sub>2</sub>O<sub>3</sub>, Bi<sub>2</sub>O<sub>3</sub>, I<sub>2</sub>O<sub>5</sub>, MnO<sub>2</sub>, WO<sub>2</sub> etc., as oxidizer showed a much higher value of energy release, even double, than the above mentioned traditional monomolecular compounds [14, 26–29].

In addition to energy release, the volume of gas generation and corresponding gas pressure plays a crucial role specially for propulsion system [30, 31]. The nano-energetic formulation including bismuth and iodine-based oxidizers showed some exceptional results of pressure discharge to work as micro-propulsion system for nano satellites with millinewtons/s thrust resolutions, as well as high power linear actuators with maximum power of 4700 W/kg when integrated over the multiwalled carbon nano tube (MWCNT) yarns [32, 33].

The development of nanocomposites incorporating silver and/or iodine-based oxidizers represents a cutting-edge approach in the realm of disinfection science. Silver nanoparticles are known for their antimicrobial ability, disrupting microbial structures, while iodine-based compounds offer broad-spectrum antimicrobial activity [33–36]. By synergistically integrating these agents into nanocomposites, the overall effectiveness against bacteria, viruses, and other pathogens is heightened. The controlled release of silver ions and iodine from the nanocomposite structure further ensures prolonged and targeted disinfection. This scientific innovation holds significant promise for applications in medical settings, water treatment, and surface coatings, showcasing a potential paradigm shift in the development of advanced disinfection materials with heightened efficacy and controlled release capabilities.

It has been observed that the oxidizer's performance also depends on the mechanical modification and synthesis approach. A study done for  $\text{Bi}_2\text{O}_3$  synthesized by liquid combustion synthesis using bismuth nitrate and glycine when used with aluminum nanoparticles as  $\text{Al-Bi}_2\text{O}_3$  nano formulation gives a significant thermal front propagation with velocity 2500 m/s and a peak pressure  $\approx 12$  MPa taking 1:4 weight stoichiometry of fuel and oxidizer [9]. Other proven methods for synthesizing nanocomposites with desired reaction output includes sol-gel, sputtering, chemical vapor deposition etc. [18]. Not only metal oxides, a recent computational and experimental studies on metal hydroxides showed some exceptional results, generating enthalpy of reaction up to  $-50.66$  kJ/cc for  $\text{Al-Ce(OH)}_4$  as well as the highest PV value of  $5.6$  kPa  $\times$  m<sup>3</sup>/g for  $\text{Al-Bi(OH)}_3$  nano formulation [16]. Regarding the maximum gas pressure, the choice of the oxidizer should be taken in such a way that it contains the metal particle whose boiling point is comparatively low so that, during product formation of such metals they start evaporating fast and hence responsible for greater gas discharge [14].

One of the biggest advantages of using nanocomposites over traditional energetic compounds is that there are ways to tune or control the energy release, pressure discharge and severity of the reaction. This advantage along with high stability and customizable sensitivity made it a major concern for the scientific community to use it as micro-electromechanical system (MEMS)

[37], which emphasizes groundbreaking intersection of nanotechnology and microsystem technology with various important applications. MEMS involve the miniaturization of mechanical and electromechanical components at the microscale, enabling the creation of compact, highly responsive devices with diverse applications. Nanocomposites, with their tunable energy release, pressure discharge, and reaction severity, emerge as key components in MEMS due to their ability to precisely control the performance characteristics of energetic materials at the micro level [38]. This integration holds immense potential for the development of MEMS-based sensors, actuators, and other devices that demand intricate control and high efficiency [39–41]. The customizable sensitivity of nanocomposites in MEMS not only enhances the performance of these microsystems but also opens up possibilities for innovative applications in fields such as aerospace, healthcare, and telecommunications. As researchers continue to explore the synergies between nanocomposites and MEMS technology, the resulting advancements hold promise for revolutionizing the field of microscale engineering and contributing to the development of next-generation, high-performance microsystems.

Moreover, the energy release, gas generation and the peak temperature pulse can be tailored to optimum level by taking a good choice of nano-sized powder of fuel and oxidizer by varying proportion to reach the perfect stoichiometry of the reactant mixtures. In addition, having a nano-scaled reacting particles have low activation energy to initiate the ignition as well as greater sensitivity to impact, friction, shock, heat etc. [42]. However, the major challenge comes with balancing between lowering the sensitivity of the materials leading to greater safety on handling and, obtaining the maximum detonation performance, especially in large scale at industry level [43–45].

It is expected to have both the fuel and oxidizer to be in nano sized dimension for better combustion rate, greater ignition temperature and greater pressure pulse. However, some recent studies have shown that the particle size of aluminum fuel to be nano-scaled is less important than the particle size of oxidizer to be in nanoscale, and, hence, having the nanosized oxidizer is an essential characteristic of thermite system [23, 46].

There are much ongoing research works aiming to get nanocomposites with high reaction enthalpy, greater pressure discharge and high thermal impulse. The electronic and optical characteristics of oxynitrides are often tunable due to the combination of oxygen and nitrogen, which makes oxynitrides suitable for applications in across various scientific and technological domains including electronic devices, optoelectronics, and photocatalysis. Particularly, their photocatalytic behavior lends itself to environmental applications, contributing to pollutant degradation and solar energy conversion.

Oxynitrides also find usefulness in energy storage systems, acting as promising materials for batteries with improved performance. Additionally, their structural variability allows for tailored properties, enabling applications in magnetic devices, catalysis, and high-temperature stability scenarios. Certain oxynitrides even exhibit superconducting properties at low temperatures, contributing to advancements in superconductor technologies. As ongoing research continues to uncover new oxynitride materials and refine their properties, the potential applications across a spectrum of technological fields remain a focus of exploration and development.

There are several ways of synthesizing the oxynitrides including thermal ammonolysis of oxides, solid-solid reactions under nitrogen environment, sol-gel etc. [47–49]. Metal oxynitrides can be used in diverse fields as they are known to possess some important optical, mechanical, and thermal properties including high wear and tear resistance, high thermal and chemical stability, and high value of dielectric constant and are also known for photocatalytic water splitting [50–52]. Additionally, metal oxynitrides have the potential to store chemical energy to use in electrodes in batteries and supercapacitors for the growing need of energy storage technology [53].

In this study, a computational thermodynamic calculation and analysis were performed for nine oxynitrides to identify some of the best oxidizer compounds to use as Al-oxynitride nanocomposites using two different computational tools THERMO [54] and HSC Chemistry 7 [55]. Oxynitrides, with their unique combination of oxygen and nitrogen, have garnered interest in the domain of energetic materials due to their potential for controlled energy release.

The incorporation of nitrogen, known for its role in high-energy compounds, offers a pathway to enhance the reactivity and explosive characteristics of these materials. The tunable nature of oxynitrides allows for the optimization of energy release and combustion properties, making them promising candidates for applications in pyrotechnics, construction, mining, and defense. However, the design and synthesis of oxynitrides as energetic materials require careful consideration of factors such as stability, sensitivity, and controllable ignition. Ongoing research in this field aims to unlock the full potential of oxynitrides in energetic materials, balancing enhanced performance with safety considerations.

## CHAPTER III

### SYSTEMS UNDER STUDY

For this research nine oxynitride compounds were taken among which five are perovskite type oxynitrides of the form  $ABO_2N$  ( $A = Ba, Sr, Ca$  and,  $B = Nb, Ta$ ). Bismuth oxynitrate hydrate,  $BiONO_3 \cdot H_2O$  was also taken for the study and rest three are linear in their chemical formula namely: sodium silicon oxynitrides, titanium nickel oxynitrides and potassium germanium oxynitrides ( $NaSiON, TiNiON, KGeON$ ).

#### 3.1 Perovskite Type of Oxynitrides, $ABO_2N$ ( $A=Ba, Sr, Ca$ and $B=Ta, Nb$ )

Perovskite-type oxynitrides, with the general formula  $ABO_2N$  (where  $A = Ba, Sr, Ca$  and  $B = Nb, Ta$ ), exhibit a distinctive crystal structure with the possibilities for diverse applications, particularly in the domain of energetic materials. The perovskite structure, featuring a network of corner-sharing octahedra, imparts unique properties to these compounds, making them intriguing for various technological advancements.

The formation of perovskite oxynitrides can be split into multiple steps as,



Where  $A \rightarrow Ba, Sr, Ca$ , and  $B \rightarrow Ta, Nb$ .

Then those nitrides and oxides combine with oxygen atom to form  $ABO_2N$  as,



There are other methods as well to synthesize such oxynitrides like ammonolysis of complex oxide precursors. The oxide precursors can be in the form  $A_2B_2O_7$  which when exposed to ammonia results in giving oxynitrides along with waters as shown below,

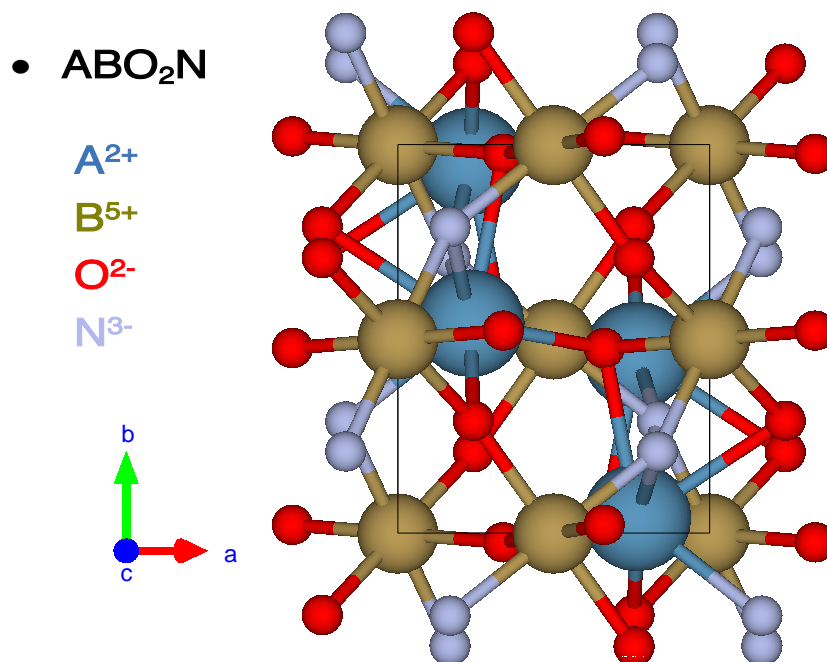


Figure 3.1: Molecular structure of perovskite metal oxynitrides of the form  $ABO_2N$ .

Figure 3.1 shows molecular crystal structure of perovskite metal oxynitrides of the form  $ABO_2N$ . For example,  $CaTaO_2N$  has an orthorhombic perovskite-derived structure and crystallizes in the orthorhombic  $Pmc_{21}$  space group [56]. There are two  $Ca^{2+}$  sites. In the first site,  $Ca^{2+}$  is bonded to four  $N^{3-}$  and four  $O^{2-}$  atoms with  $Ca-N$  bond lengths of 2.49 Å and 2.60 Å, and  $Ca-O$  bond lengths ranging from 2.34 Å to 2.79 Å. In the second site,  $Ca^{2+}$  is bonded to two  $N^{3-}$  and six  $O^{2-}$  atoms, with  $Ca-N$  bond lengths of 2.85 Å and  $Ca-O$  bond lengths from 2.37 Å to 2.64 Å.  $Ta^{5+}$  is bonded to two  $N^{3-}$  and four  $O^{2-}$  atoms forming  $TaN_2O_4$  octahedra, with  $Ta-N$  bond lengths of 1.94 Å and 2.02 Å, and  $Ta-O$  bond lengths from 2.03 Å to 2.21 Å.  $N^{3-}$

is bonded to three  $\text{Ca}^{2+}$  and two  $\text{Ta}^{5+}$  atoms. There are three  $\text{O}^{2-}$  sites, each bonded to  $\text{Ca}^{2+}$  and  $\text{Ta}^{5+}$  atoms in varying geometries, forming distorted  $\text{OCa}_2\text{Ta}_2$  tetrahedra.

Similarly,  $\text{CaNbO}_2\text{N}$  has an orthorhombic perovskite-derived structure [56] and crystallizes in the monoclinic  $\text{P}_{21}/c$  space group. The  $\text{Ca}^{2+}$  ions are bonded to three  $\text{N}^{3-}$  and five  $\text{O}^{2-}$  ions, with  $\text{Ca}-\text{N}$  bond lengths between 2.44–2.80 Å and  $\text{Ca}-\text{O}$  bond lengths between 2.39–2.89 Å.  $\text{Nb}^{5+}$  ions occupy two distinct sites, both forming  $\text{NbN}_2\text{O}_4$  octahedra with similar bond lengths and tilt angles of 27–30°. The  $\text{N}^{3-}$  ions are bonded to three  $\text{Ca}^{2+}$  ions and two  $\text{Nb}^{5+}$  ions, while  $\text{O}^{2-}$  ions are found in two sites, each bonded to  $\text{Ca}^{2+}$  and  $\text{Nb}^{5+}$  ions, forming corner-sharing tetrahedra and 5-coordinate geometries.

$\text{BaTaO}_2\text{N}$  has a cubic perovskite-derived structure [57] and crystallizes in the tetragonal  $\text{P}_4/\text{mmm}$  space group.  $\text{Ba}^{2+}$  is coordinated to four  $\text{N}^{3-}$  and eight  $\text{O}^{2-}$  atoms, forming  $\text{BaN}_4\text{O}_8$  cuboctahedra that share corners with twelve, faces with six other  $\text{BaN}_4\text{O}_8$  cuboctahedra, and faces with eight  $\text{TaN}_2\text{O}_4$  octahedra. The  $\text{Ba}-\text{N}$  and  $\text{Ba}-\text{O}$  bond lengths are both 2.92 Å and 2.93 Å, respectively.  $\text{Ta}^{5+}$  is coordinated to two  $\text{N}^{3-}$  and four  $\text{O}^{2-}$  atoms, forming  $\text{TaN}_2\text{O}_4$  octahedra that share corners with six other  $\text{TaN}_2\text{O}_4$  octahedra and faces with eight  $\text{BaN}_4\text{O}_8$  cuboctahedra. The  $\text{Ta}-\text{N}$  and  $\text{Ta}-\text{O}$  bond lengths are both 2.07 Å, and the octahedra are not tilted.  $\text{N}^{3-}$  is in a distorted linear geometry, bonded to four  $\text{Ba}^{2+}$  and two  $\text{Ta}^{5+}$  atoms. Similarly,  $\text{O}^{2-}$  is bonded in a distorted linear geometry to four  $\text{Ba}^{2+}$  and two  $\text{Ta}^{5+}$  atoms.

$\text{SrNbO}_2\text{N}$  is very much similar in structure with  $\text{BaTaO}_2\text{N}$ , a cubic perovskite-derived structure crystallizing in the tetragonal  $\text{P}_4/\text{mmm}$  space group.  $\text{Sr}^{2+}$  is bonded to four  $\text{N}^{3-}$  and eight  $\text{O}^{2-}$  atoms, forming  $\text{SrN}_4\text{O}_8$  cuboctahedra. These share corners with twelve, faces with six other  $\text{SrN}_4\text{O}_8$  cuboctahedra, and faces with eight  $\text{NbN}_2\text{O}_4$  octahedra. All  $\text{Sr}-\text{N}$  bond lengths are 2.89 Å, and all  $\text{Sr}-\text{O}$  bond lengths are 2.90 Å.  $\text{Nb}^{5+}$  is bonded to two  $\text{N}^{3-}$  and four  $\text{O}^{2-}$  atoms, forming  $\text{NbN}_2\text{O}_4$  octahedra that share corners with six equivalent octahedra and faces with eight  $\text{SrN}_4\text{O}_8$  cuboctahedra. The  $\text{Nb}-\text{N}$  bond lengths are 2.05 Å, and the  $\text{Nb}-\text{O}$  bond lengths are 2.04 Å.  $\text{N}^{3-}$  is in a distorted linear geometry, bonded to four  $\text{Sr}^{2+}$  and two  $\text{Nb}^{5+}$  ions, while  $\text{O}^{2-}$  ions also adopt a distorted linear geometry, bonding to four  $\text{Sr}^{2+}$  and two  $\text{Nb}^{5+}$  ions.

On the other hand SrTaO<sub>2</sub>N crystallizes in the tetragonal I<sub>4</sub>/mcm space group [56]. Sr<sup>2+</sup> is bonded to four N<sup>3-</sup> and eight O<sup>2-</sup> atoms, forming distorted SrN<sub>4</sub>O<sub>8</sub> cuboctahedra. These share corners with twelve, faces with six other SrN<sub>4</sub>O<sub>8</sub> cuboctahedra, and faces with eight TaN<sub>2</sub>O<sub>4</sub> octahedra. The Sr–N bond lengths are 2.84 Å. Sr–O bond lengths vary, with four shorter bonds at 2.64 Å and four longer bonds at 3.14 Å. Ta<sup>5+</sup> is bonded to two N<sup>3-</sup> and four O<sup>2-</sup> atoms, forming TaN<sub>2</sub>O<sub>4</sub> octahedra that share corners with six equivalent octahedra and faces with eight SrN<sub>4</sub>O<sub>8</sub> cuboctahedra. The octahedral tilt angles range from 0-20°. Both Ta–N bond lengths are 2.06 Å, and all Ta–O bond lengths are 2.04 Å. N<sup>3-</sup> is in a distorted linear geometry, bonded to four Sr<sup>2+</sup> and two Ta<sup>5+</sup> ions, while O<sup>2-</sup> ions adopt a 4-coordinate geometry, bonding to four Sr<sup>2+</sup> and two Ta<sup>5+</sup> ions.

In general, perovskite oxynitrides find applications in photocatalysis, optoelectronics, and energy storage. Their tunable electronic band structure, influenced by the choice of alkaline earth metals (A) and transition metals (B), makes them versatile materials for tailoring properties like bandgap and charge carrier mobility. In the context of energetic materials, perovskite-type oxynitrides hold promise due to their ability to undergo controlled exothermic reactions, making them suitable for applications in propulsion systems, pyrotechnics, and explosives. The tailored electronic properties of these materials, stemming from the specific combinations of A and B elements, contribute to their energetic potential. For instance, the controlled release of energy during combustion or reaction processes can be harnessed for efficient propulsion systems or as components in advanced pyrotechnic formulations.

Moreover, the compatibility of perovskite oxynitrides with nanotechnology opens path for the development of nano-energetic systems. Manipulating these materials at the nanoscale allows for enhanced reactivity and efficiency, crucial factors in optimizing energetic performance. The integration of perovskite oxynitrides into nanostructured energetic materials represents a frontier where their unique properties can be a strong match for cutting-edge applications in energy release and storage.

### 3.2 Bismuth Oxynitrate Hydrate (BiONO<sub>3</sub>·H<sub>2</sub>O)

Bismuth oxynitrate hydrate, often represented as BiONO<sub>3</sub>·H<sub>2</sub>O, also called bismuth sub-nitrate, is a chemical compound that includes bismuth (Bi), oxygen (O), nitrogen (N), and water molecules (H<sub>2</sub>O) in its composition and are formed by the chemical reaction:



This compound is part of the broader category of oxynitrides, characterized by the presence of both oxygen and nitrogen in their structure. Bismuth oxynitrate hydrate is known for its distinctive properties and potential applications. Bismuth is a heavy metal with various oxidation states. In bismuth oxynitrate, it often adopts the +3-oxidation state. In the structure, oxygen contributes as oxide ions (O<sup>2-</sup>) whereas nitrogen, in the form of nitrate NO<sub>3</sub><sup>-</sup>. The inclusion of water molecules, H<sub>2</sub>O, indicates that the compound exists in a hydrated form which can influence the chemical and physical properties of the compound. Bismuth compounds are known for their various applications, including in pharmaceuticals, pigments, and as catalysts. They may be explored for applications in environmental remediation or solar energy conversion.

### 3.3 Potassium Germanium Oxynitride (KGeON)

KGeON can be obtained by reacting potassium oxide with nitrides and oxides of germanium and can be represented in chemical equation as,



Figure 3.2 below shows KGeON crystallizing in the orthorhombic Pca<sub>21</sub> space group [58]. K<sup>1+</sup> is bonded in a 6-coordinate geometry to one N<sup>3-</sup> ion and five equivalent O<sup>2-</sup> ions. The K–N bond length is 2.87 Å, with K–O bond distances ranging from 2.70 Å to 3.04 Å. Ge<sup>4+</sup> is bonded to three equivalent N<sup>3-</sup> ions and one O<sup>2-</sup> ion, forming corner-sharing GeN<sub>3</sub>O tetrahedra.

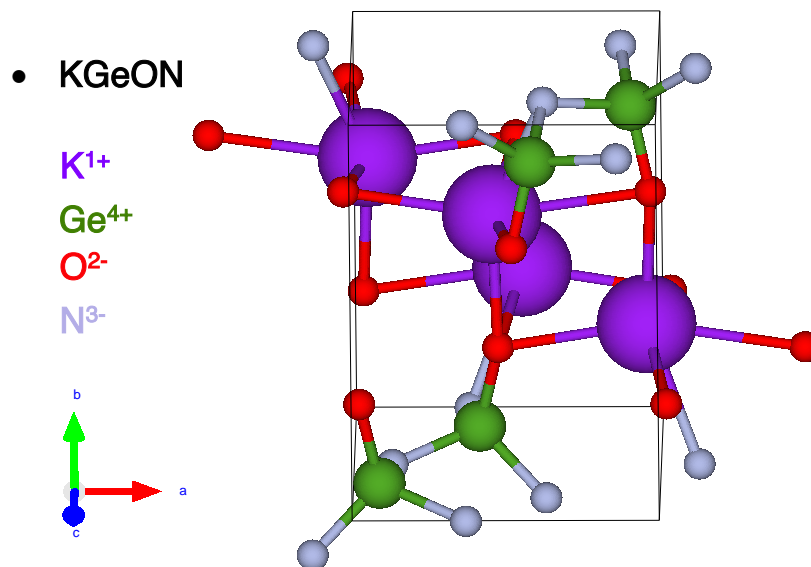
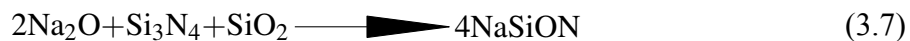


Figure 3.2: Molecular crystal structure of potassium germanium oxynitrides (KGeON).

The Ge–N bond lengths are 1.88 Å (shorter) and 1.89 Å (longer), while the Ge–O bond length is 1.76 Å. N<sup>3-</sup> ions are bonded to one K<sup>1+</sup> ion and three equivalent Ge<sup>4+</sup> ions, forming distorted corner-sharing NKGe<sub>3</sub> trigonal pyramids. O<sup>2-</sup> is in a 6-coordinate geometry, bonded to five equivalent K<sup>1+</sup> ions and one Ge<sup>4+</sup> ion.

### 3.4 Sodium Silicon Oxynitride (NaSiON)

Sodium silicon oxynitride, NaSiON, is a compound that contains sodium (Na), silicon (Si), oxygen (O), and nitrogen (N) and reacting oxide of sodium with nitride and oxide of silicon is one of the ways to obtain them, which can be expressed in chemical reaction as,



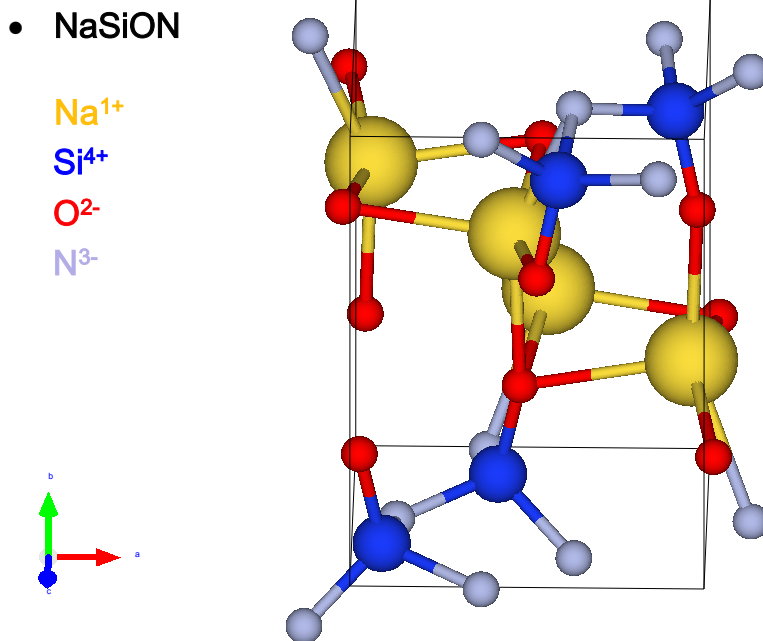


Figure 3.3: Molecular structure of sodium silicon oxynitrides (NaSiON).

NaSiON has the chemical structure [57] similar to KGeON and is known for its interesting properties, combining elements from sodium, silicon, oxygen, and nitrogen as shown in Figure 3.3 above. It is commonly employed in the production of glass and ceramics, where its unique properties contribute to improved thermal stability and resistance to chemical corrosion. The compound exhibits tunable optical and electrical properties, making it valuable in various applications, including as a component in advanced materials for electronic devices and coatings. Generally, sodium oxynitrides can be used in applications ranging from materials science to energy storage

### 3.5 Titanium Nickel Oxynitride (TiNiON)

Titanium nickel oxynitride (TiNiON) is a compound that belongs to the family of oxynitrides, featuring titanium (Ti), nickel (Ni), oxygen (O), and nitrogen (N) in its composition and can be obtained by reacting nickel oxide and titanium nitride.



This material is of particular interest due to its potential applications in various technological fields. The combination of transition metals like titanium and nickel with oxygen and nitrogen allows for tunable electronic and structural properties, making TiNiON suitable for applications in electronic devices, sensors, and possibly energetic materials. The specific properties of TiNiON, such as its electronic band structure and stability, are crucial factors in determining its performance in different applications.

## CHAPTER IV

### METHODOLOGY

#### 4.1 Thermodynamic Calculations

Thermodynamic calculation plays significant role in estimating the energy release out of the nanocomposite combustion. The nano sized particle mixture is vital for having less activation energy so that even a small trigger can initiate the burning and leads to complete combustion in short time. Calculation for adiabatic combustion temperature, gas discharge pressure and energy release out of the exothermic reaction, was done taking two different software, namely: THERMO [54] and HSC Chemistry 7 [55]. THERMO works based on minimization of thermodynamic potential: Gibbs free energy, leading to generate calculation taking most stable reaction possible. It gives the equilibrium concentration of products with their corresponding concentration and phase as well as the volume of gas generated out of the chemical reaction provided that the initial concentration of reactants, their phases, temperatures, and amounts are given as input. Moreover, it gives the estimation for an important thermodynamic parameter when two or more reactant gets burned: the adiabatic combustion temperature, which has significant impact in releasing high energy from point of ignition. THERMO consist of the database of over 3000 compounds and predicts for the equilibrium products to the given input reactants.

For a system with  $N(g)$  number of gas and  $N(s)$  number of solid components, the concentration of equilibrium phases at constant pressure is given as,

$$F(\{n_k\}, \{n_s\}) = \sum_{k=1}^{N(g)} n_k \left( \ln \frac{p_k}{P} + G_k \right) + \sum_{l=1}^{N(s)} n_l G_l \quad (4.1)$$

Where,  $p_k$  is the partial pressure of  $k^{th}$  gas phase component,  $n_l$  and  $G_l$  are the number of

moles and molar Gibbs free energy of the components. The adiabatic combustion temperature is determined taking the total energy balance given as,

$$\sum_{i=1}^{N_0} H_i(T_0) = \sum_{k=1}^{N(g)} n_k H_k(T_c^{\text{ad}}) + \sum_{l=1}^{N(s)} n_l H_l(T_c^{\text{ad}}) \quad (4.2)$$

Where the enthalpy of each component is expressed as,

$$H_i(T) = \Delta H_{f,i}^0 + \int_{T_0}^T c_{p,i} dT + \sum \Delta H_{s,i} \quad (4.3)$$

and  $\Delta H_{f,i}^0$  is the heat of formation at 1 atm pressure and reference temperature  $T_0$ ,  $c_{p,i}$  is the heat capacity, and  $\Delta H_{(s,i)}$  is the heat of formation of s-th phase transition for the components.

HSC Chemistry stands as a robust and comprehensive software package developed by Metso Outotec, a company working in minerals and metals processing technology. One of its primary strengths lies in thermodynamic modeling, offering a wide array of thermodynamic databases covering elements, compounds, and reactions. This capability enables to simulate and analyze intricate chemical processes under varying conditions, considering factors such as temperature, pressure, and composition. The software excels in process simulation, making it an invaluable resource for modeling complex chemical processes like mineral processing, hydrometallurgy, and pyrometallurgy. Equilibrium calculations for multicomponent systems are a fundamental feature, predicting the distribution of elements and compounds in different phases. HSC Chemistry extends its utility to the generation of phase diagrams, providing graphical representations of stability regions for different phases, essential for understanding material behavior under diverse environments.

Beyond thermodynamics, the software encompasses kinetics modeling, allowing users to comprehend and predict reaction rates over time. The materials database included in HSC Chemistry covers a spectrum of thermophysical and transport properties, aiding in materials selection and process optimization. A notable feature is the ability to customize thermodynamic databases,

empowering users to incorporate their own experimental data for a tailored approach. The software's integration capabilities with other tools and databases enhance its adaptability, fostering a holistic approach to chemical process analysis and design. Recognized for its accuracy and reliability, HSC Chemistry stands at the forefront of software applications dedicated to predicting the thermodynamics and kinetics of intricate chemical systems, making significant contributions to research and development efforts in industries dealing with chemical processes and materials. Thermodynamic parameters along with products and their phases, for each exothermic reactions were calculated by varying the concentration of aluminum fuel by a factor of 0.1 mole, keeping oxynitride constant to one mole. With this the adiabatic combustion temperature and volume of gas generation in each chemical reaction were observed for each varied stoichiometry of the reactants. Out of several number of trails of the varied reactants, the reaction stoichiometry with greatest values of combustion temperature and gas generation are of the interest of this study. Then the inputs and corresponding outputs from THERMO are feed into the HSC Chemistry, to obtain the estimated value of gravimetric and volumetric energy release out of the chemical reaction from Al/oxynitride composites.

In addition to these thermodynamic calculations, the study was extended to take account of electronic structure calculations of the oxidizer compounds in order to get an insight of the relation between their energetic nature and electronic structures. As a safety measure it is important to know the sensitivity of these composites to external sources including its exposure to lights. Moreover, knowing the optical interaction of such systems can also be helpful in triggering the initial reaction using light source in such a system. For this the first principle approach was implemented using *Vienna Ab initio Simulation Package* (VASP). VASP is a computational tool used for modeling materials at the atomic scale, including electronic structure calculations and quantum-mechanical molecular dynamics, all from first principles. In VASP, essential quantities such as one-electron orbitals, electronic charge density, and local potential are represented using plane wave basis sets.

## 4.2 Overview of Density Functional Theory (DFT)

A computational quantum mechanical modeling technique called density functional theory (DFT) [59] is used to study the electronic structure, or more specifically, the ground state, of many-body systems, including atoms, molecules, and solids. Because it derives quantities directly from established equations of quantum mechanics and electromagnetism, without relying on empirical parameters or experimental data, it is referred to as a “first principles” or “ab initio” method. The fundamental principle of DFT is to rewrite the complex many-electron wavefunction in terms of the electron density, rather than the many-body wavefunction for each of the electrons in a system, and hence reformulating the many-body Schrödinger equation. One of the foundational equations of quantum mechanics, the Schrödinger equation explains how a physical system’s quantum state varies over space and time. It is the fundamental formula for explaining the actions of quantum particles, including electrons in atoms and molecules.

### 4.2.1 Forms of the Schrödinger Equation:

#### 1. Time-Dependent Schrödinger Equation:

This form describes how the quantum state of a system evolves over time. It is given by:

$$i\hbar \frac{\partial \Psi(\mathbf{r}, t)}{\partial t} = \hat{H} \Psi(\mathbf{r}, t) \quad (4.4)$$

where:

- $i$  is the imaginary unit.
- $\hbar$  is the reduced Planck’s constant ( $\hbar = \frac{h}{2\pi}$ ).
- $\Psi(\mathbf{r}, t)$  is the wave function of the system, which depends on position  $\mathbf{r}$  and time  $t$ .
- $\hat{H}$  is the Hamiltonian operator, representing the total energy of the system.

## 2. Time-Independent Schrödinger Equation:

When the system's Hamiltonian is not dependent on time, the time-independent Schrödinger equation is used. This form is typically used for stationary states, where the system's energy is constant. It is given by:

$$\hat{H}\Psi(\mathbf{r}) = E\Psi(\mathbf{r}) \quad (4.5)$$

where:

- $\Psi(\mathbf{r})$  is the spatial part of the wave function.
- $E$  is the energy eigenvalue associated with the wave function  $\Psi(\mathbf{r})$ .

### 4.2.2 Theoretical Foundations of DFT

- First Hohenberg-Kohn Theorem:

The first theorem states that the ground state properties of a many-electron system are uniquely determined by its functional of electron density  $\rho(\mathbf{r})$ . Formally, it asserts that the external potential  $V_{\text{ext}}(\mathbf{r})$  is a unique functional of the electron density  $\rho(\mathbf{r})$ . Consequently, the ground state wavefunction  $\Psi$  and all other properties of the system are determined by  $\rho(\mathbf{r})$ .

$$V_{\text{ext}}(\mathbf{r}) \rightarrow \rho(\mathbf{r}) \rightarrow \Psi \rightarrow \text{all properties}$$

- Second Hohenberg-Kohn Theorem:

The second Hohenberg-Kohn theorem states that the electron density  $n(\mathbf{r})$  that minimizes the energy of a functional is the true electron density corresponding to the full solution of the Schrödinger equation. If the exact functional form were known, one could vary the electron density until the energy from the functional is minimized, providing a method to find the correct electron density.

The energy functional  $E[\{\psi_i\}]$  can be expressed in terms of single-electron wave functions  $\psi_i(r)$ :

$$E[\{\psi_i\}] = E_{\text{known}}[\{\psi_i\}] + E_{\text{XC}}[\{\psi_i\}] \quad (4.6)$$

where,  $E_{\text{known}}[\{\psi_i\}]$  includes the known contributions:

$$E_{\text{known}}[\{\psi_i\}] = \langle \psi_i | -\frac{\hbar^2}{2m} \nabla^2 + V(r) | \psi_i \rangle + \int V(r) n(r) d^3 r + \frac{e^2}{2} \iint \frac{n(r)n(r')}{|r-r'|} d^3 r d^3 r' + E_{\text{ion}} \quad (4.7)$$

The exchange-correlation functional  $E_{\text{XC}}[\{\psi_i\}]$  encompasses all quantum mechanical effects not explicitly included in  $E_{\text{known}}[\{\psi_i\}]$ .

- Kohn-Sham Equations:

Density Functional Theory (DFT) use in practice relies heavily on the Kohn-Sham equations. They enable us to transfer the ground-state electron density of a complex interacting many-electron system onto a simpler non-interacting electron system. With this method, it is possible to compute the electronic characteristics of a variety of systems, including solids, molecules, and atoms. Kohn and Sham introduced a practical solution by formulating the Kohn-Sham equations:

$$\left[ -\frac{\hbar^2}{2m} \nabla^2 + V(r) + V_H(r) + V_{\text{XC}}(r) \right] \psi_i(r) = \epsilon_i \psi_i(r) \quad (4.8)$$

These equations resemble the Schrödinger equation but are formulated for single-electron wave functions  $\psi_i(r)$  dependent on three spatial variables.  $V(r)$  is the external potential,  $V_H(r)$  is the Hartree potential due to electron-electron interactions, and  $V_{\text{XC}}(r)$  is the exchange-correlation potential.

The Hartree potential must be defined in order to solve the Kohn-Sham equations, and knowing the electron density is necessary in order to define the Hartree potential. However, in order to determine the electron density, we need to solve the Kohn-Sham equations

in order to obtain the single-electron wave functions. In order to break this cycle, the issue is typically approached iteratively, as demonstrated by the algorithm that follows:

1. Define an initial, trial electron density,  $n(\mathbf{r})$ .
2. Solve the Kohn-Sham equations using the trial electron density to find the single-particle wave functions,  $\psi_i(\mathbf{r})$ .
3. Calculate the electron density defined by the Kohn-Sham single-particle wave functions from step 2,  $n_{\text{KS}}(\mathbf{r})$ , given by:

$$n_{\text{KS}}(\mathbf{r}) = 2 \sum_i |\psi_i(\mathbf{r})|^2 \quad (4.9)$$

4. Examine the difference between the electron density utilized to solve the Kohn-Sham equations,  $n(\mathbf{r})$ , and the computed electron density,  $n_{\text{KS}}(\mathbf{r})$ . This is the ground-state electron density, and it can be used to calculate the total energy if the two densities are equal. The trial electron density needs to be updated in some way if the two densities differ. After completing this, step 2 of the procedure is repeated.

- Exchange Correlation Functionals:

In Density Functional Theory (DFT), the exchange-correlation functional  $E_{\text{XC}}[\rho]$  is crucial for accurately describing the many-body interactions among electrons. Different approximations are used to represent  $E_{\text{XC}}[\rho]$ :

1. Local Density Approximation (LDA): The Local Density Approximation (LDA) is one of the simplest approximations for the exchange-correlation functional. It assumes that the exchange-correlation energy density at any point in space depends only on the local electron density, as in a homogeneous electron gas.

Mathematically, the LDA exchange-correlation energy functional is expressed as:

$$E_{\text{XC}}^{\text{LDA}}[\rho] = \int \rho(\mathbf{r}) \epsilon_{\text{XC}}^{\text{unif}}(\rho(\mathbf{r})) d\mathbf{r} \quad (4.10)$$

where  $\varepsilon_{XC}^{\text{unif}}(\rho)$  is the exchange-correlation energy per electron of a uniform electron gas with density  $\rho$ .

2. Generalized Gradient Approximation (GGA): The Generalized Gradient Approximation (GGA) improves upon LDA by taking into account the gradient of the electron density. This provides a more accurate description for systems where the electron density varies significantly in space.

The GGA exchange-correlation energy functional is given by:

$$E_{XC}^{\text{GGA}}[\rho] = \int f(\rho(\mathbf{r}), \nabla\rho(\mathbf{r})) d\mathbf{r} \quad (4.11)$$

where  $f(\rho, \nabla\rho)$  is a function that depends on both the local density  $\rho$  and its gradient  $\nabla\rho$ .

3. Hybrid Functionals: Hybrid functionals combine the exact exchange energy from Hartree-Fock theory with exchange-correlation functionals like LDA or GGA. This approach mixes a portion of the exact exchange energy with the approximate exchange-correlation energy to achieve better accuracy.

A typical hybrid functional can be written as:

$$E_{XC}^{\text{hybrid}}[\rho] = \alpha E_X^{\text{exact}} + (1 - \alpha) E_X^{\text{GGA}} + E_C^{\text{GGA}} \quad (4.12)$$

where:

$E_X^{\text{exact}}$  is the exact exchange energy from Hartree-Fock theory,  $E_X^{\text{GGA}}$  and  $E_C^{\text{GGA}}$  are the GGA exchange and correlation energies, respectively and  $\alpha$  is a mixing parameter determining the proportion of exact exchange energy.

## CHAPTER V

### RESULTS AND DISCUSSIONS

Understanding chemical reactions and their thermodynamic analysis is crucial for predicting reaction behavior, designing chemical processes, and identifying the energy changes involved in chemical transformations and gas discharge. The thermodynamic calculations performed considering the heat of reaction, peak combustion temperature and gas discharge values showed a good result to use the metal oxynitride as a high-density energetic material. The major concern lies on the prediction of the amount of gas generation, adiabatic combustion temperature, equilibrium concentration of reaction products, energy release of the exothermic chemical reaction that will support specific practical applications.

#### **5.1 Chemical Reactions and Thermodynamic Analysis**

##### **5.1.1 Equilibrium Concentration of Products and Adiabatic Combustion Temperature**

Figure 5.1 shows the adiabatic combustion temperature as well as the change in the equilibrium concentration of the reaction products as the ratio of fuel to oxidizer changes for Al/BiONO<sub>3</sub>·H<sub>2</sub>O system. The combustion temperature starts increasing from 436 K for 0.1 mole of aluminum and reaches sharply up to 1790 K and then slowly increases until 8 wt.% of aluminum. The reaction showed extreme combustion temperature with value above 3600 K when the weight percentage of fuel starts increasing over 19%. During the variation of reactant fuels up to 26 wt.%, the major gases products observed were O<sub>2</sub>(g), Bi(g), H<sub>2</sub>O(g), H(g), N<sub>2</sub>(g), H(g) and O(g). Moreover, the water in the gases form appeared from the beginning of the variation of fuel with value equal to 1 mole which then starts decreasing uniformly beyond 10 wt.% of the fuel. The O<sub>2</sub>(g) showed similar values and nature as water in gases form. As the combustion temperature starts increasing

decomposition and separation of bismuth occurs which started from around 5 wt.% of aluminum and after around 13 wt.%, the values remained constant. Also, the decomposition of nitrogen gas occurs from the beginning and remained constant of around 0.5 moles throughout the variation of the reactant fuels.

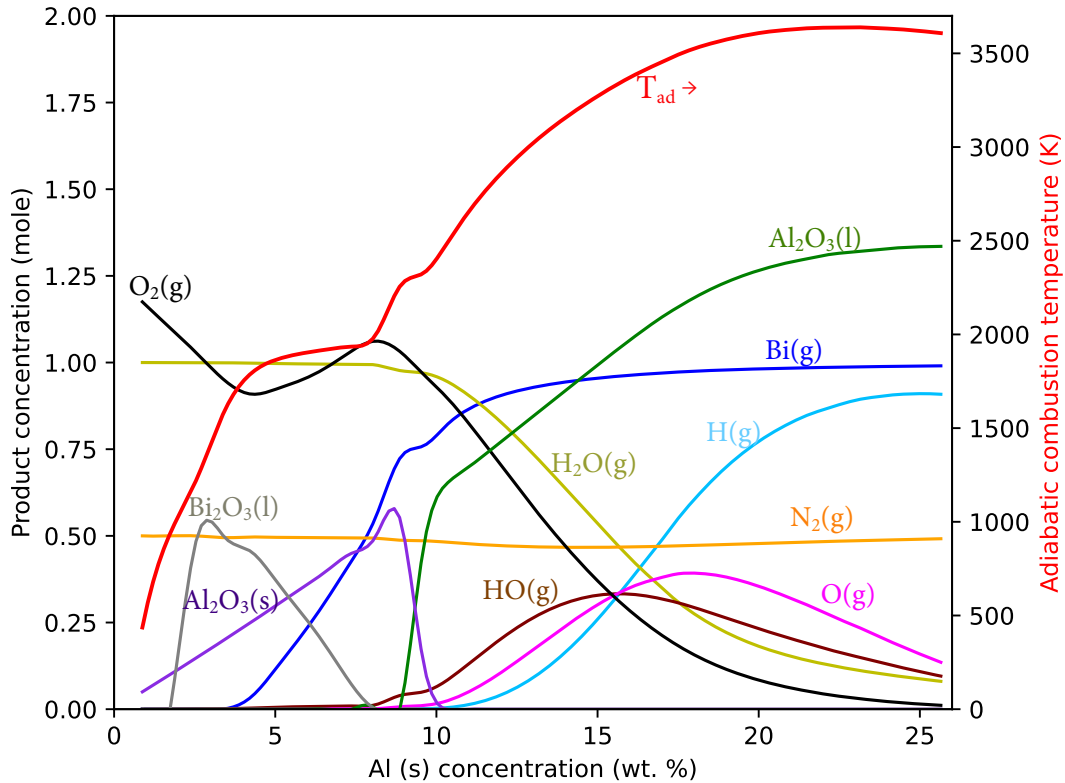


Figure 5.1: Adiabatic combustion temperature and equilibrium concentration of reaction products by varying the fuel to oxidizer ratio for Al/BiONO<sub>3</sub>·H<sub>2</sub>O system.

Figure 5.2 demonstrates dependence of adiabatic combustion temperature and equilibrium concentration of reaction products on the fuel to oxidizer ratio for Al/CaTaO<sub>2</sub>N system. The combustion temperature seemed high initially with 1 wt.% fuel concentration and goes even higher on increasing the fuel reaching maximum value of 3187 K with stoichiometry of 7.5 wt.% of fuel and then starts decreasing and finally remained constant until 24 wt.% of Al fuel. During the tuning of reactants proportion of fuel and oxidizer from 1 wt.% of aluminum to 24 wt.%, it generates so huge temperature pulse that compounds like CaO, Al<sub>2</sub>O<sub>3</sub> and even compound with tantalum, Ta<sub>2</sub>N, appeared in melted liquid state with various concentration, which on further increasing alu-

minimum concentration decreases the temperature and gives rise to gaseous products in the form of Ca,  $\text{Al}_2\text{O}_3$ ,  $\text{Al}_2\text{O}$ , and Al.

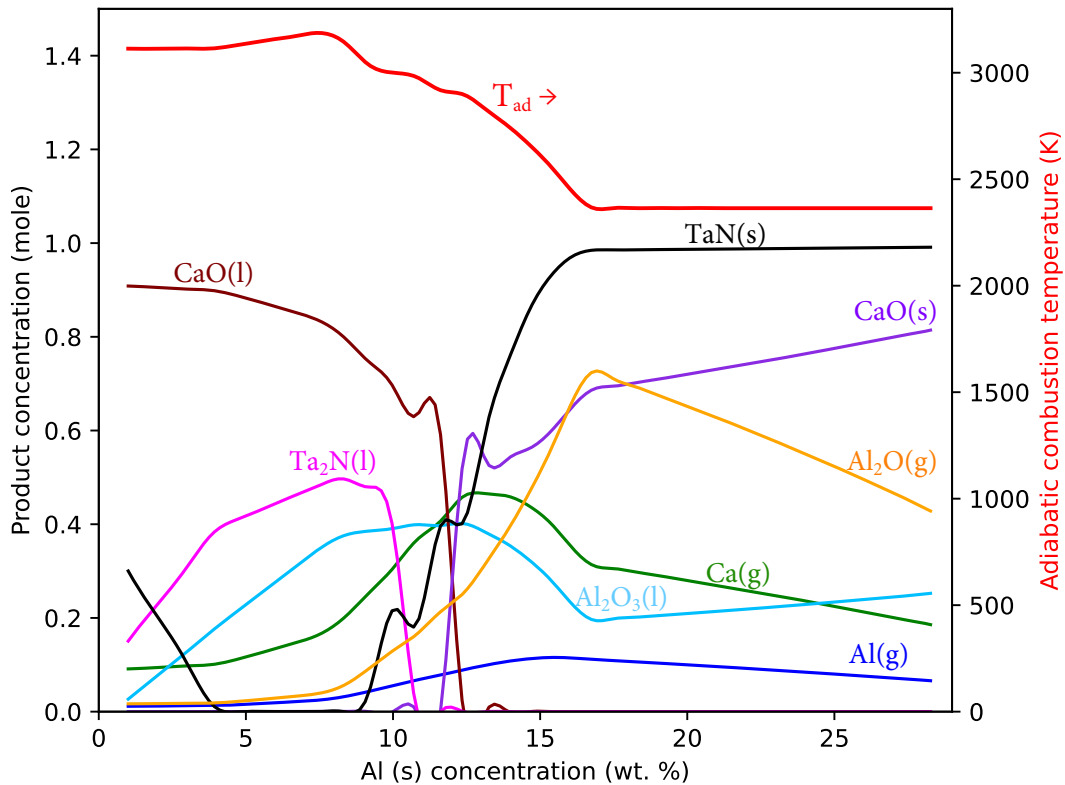


Figure 5.2: Adiabatic combustion temperature and equilibrium concentration of reaction products by varying the fuel to oxidizer ratio for Al/CaTaO<sub>2</sub>N system.

Tantalum with very high melting point of more than 3000 K, however, cannot stay in liquid form and starts freezing, forming solid TaN, with further increase in aluminum as the combustion temperature decreases below 3000 K. Moreover, the reaction scenario shown in figure 5.3 for Al/CaNbO<sub>2</sub>N is very similar to Al/CaTaO<sub>2</sub>N with peak combustion temperature of 3165 K, but since the niobium has less melting temperature than tantalum, there is no solid niobium compound even though the temperature starts decreasing. The calcium oxide (CaO) in liquid phase appeared high, 0.9 mole, in the beginning of the stoichiometry then starts decreasing and finally drops to zero after 17 wt.% of the fuel while the niobium nitride (NbN) in liquid phase appeared with 0.55 mole, fluctuates a little, reaches the maximum of 1 mole and finally decreases sharply beyond 21 wt.% of the fuel.

The other forms of liquid are aluminum oxide ( $\text{Al}_2\text{O}_3$ ) which formed from the beginning of the stoichiometry, reaching maximum value of 0.44 mole and tri-aluminum niobium ( $\text{Al}_3\text{Nb}$ ) which appeared beyond 20 wt.% of fuel along with niobium (Nb) which appeared between 7 wt.% to 19 wt.% of the fuel. During the exothermic reaction of these fuel with varying stoichiometry the gases forms are of nitrogen, calcium and aluminum oxide that appeared from the beginning until the point of maximum applied fuel.

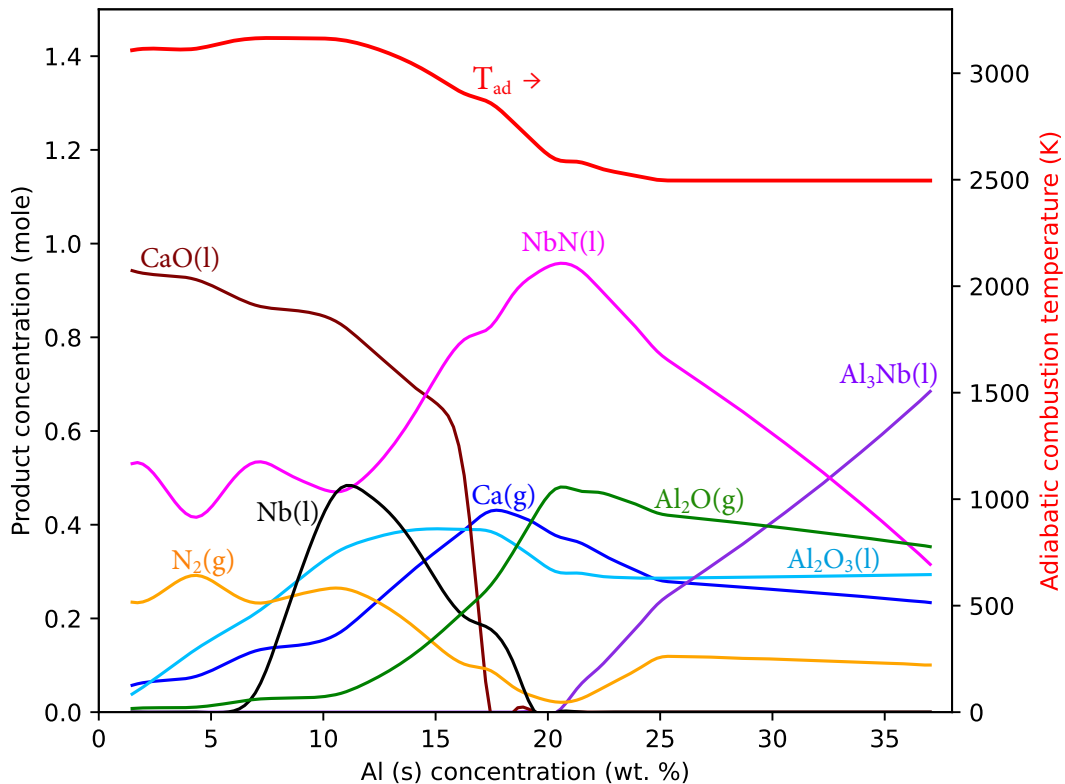


Figure 5.3: Adiabatic combustion temperature and equilibrium concentration of reaction products by varying the fuel to oxidizer ratio for  $\text{Al}/\text{CaNbO}_2\text{N}$  system.

Similarly, for  $\text{Al}/\text{SrNbO}_2\text{N}$  (presented in Figure 5.4) the maximum adiabatic combustion temperature appeared to be 3078 K corresponding to 7.70 wt.% of the fuel. The combustion temperature decreases uniformly up to 19 wt.% of the fuel and remains constant with value around 2300 K. During the entire variation of the reactant's ratio, only liquid and gases phases appeared but not the solid phase. The aluminum oxide ( $\text{Al}_2\text{O}_3$ ) in liquid phase appeared from the beginning with very small amount which then increases sharply up to 0.6 moles corresponding to 15

wt.% of the fuel and remains constant beyond 15 wt.% of the fuel. On the other hand, NbN in liquid phase appeared from the beginning, reaches the maximum with value 1 mole corresponding to 17 wt.% of the aluminum fuel and then decreases sharply. The other liquid forms appeared are NbO, SrO and Al<sub>3</sub>Nb. Regarding the gas phase, Sr (g) contributed the most, produced from the very beginning and increases sharply up to 1 mole corresponding to 15 wt.% of the fuel and then remains constant of 1 mole. The other gas phases are the oxide of aluminum (Al<sub>2</sub>O) as well as a small amount of nitrogen (N<sub>2</sub>).

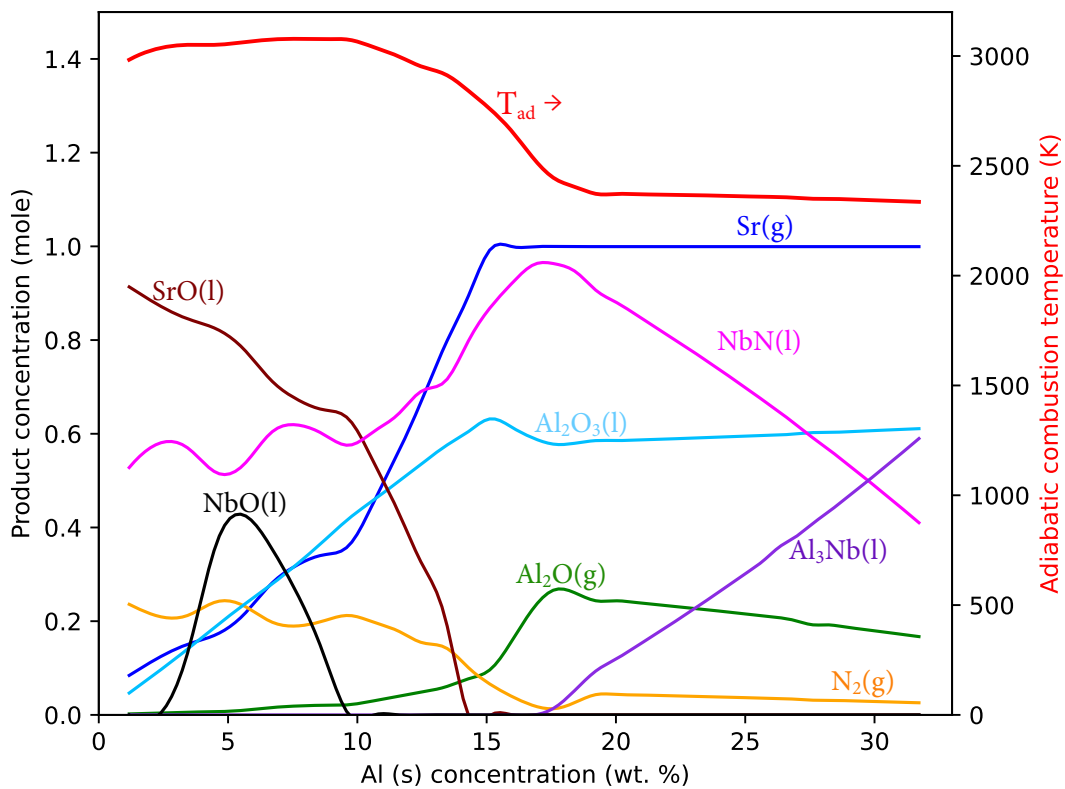


Figure 5.4: Adiabatic combustion temperature and equilibrium concentration of reaction products by varying the fuel to oxidizer ratio for Al/SrNbO<sub>2</sub>N system.

Figure 5.5 shows dependence of adiabatic combustion temperature and equilibrium concentration of reaction products on the fuel to oxidizer ratio for Al/SrTaO<sub>2</sub>N system. The maximum temperature generated was 3058 K with 7.17 wt.% of the aluminum fuel which then decreases as the aluminum concentration is increased until 19 wt.% of the fuel and finally remains constant throughout the variation of the reactant's concentration. The reaction products during



volves high concentration of Sr along with nitrogen ( $N_2$ ) and aluminum oxide ( $Al_2O_3$ ). The Sr in gas phase appeared from the beginning which then increased slowly up to 8 wt.% of fuel and then increased sharply reaching value of 1 mole remained constant beyond 12 wt.% of the fuel. Similarly, nitrogen gas appeared from the beginning with 0.2 moles which then remain somewhat constant until 9 wt.% of the fuel and then decreases to zero corresponding to 15 wt.% of the fuel.

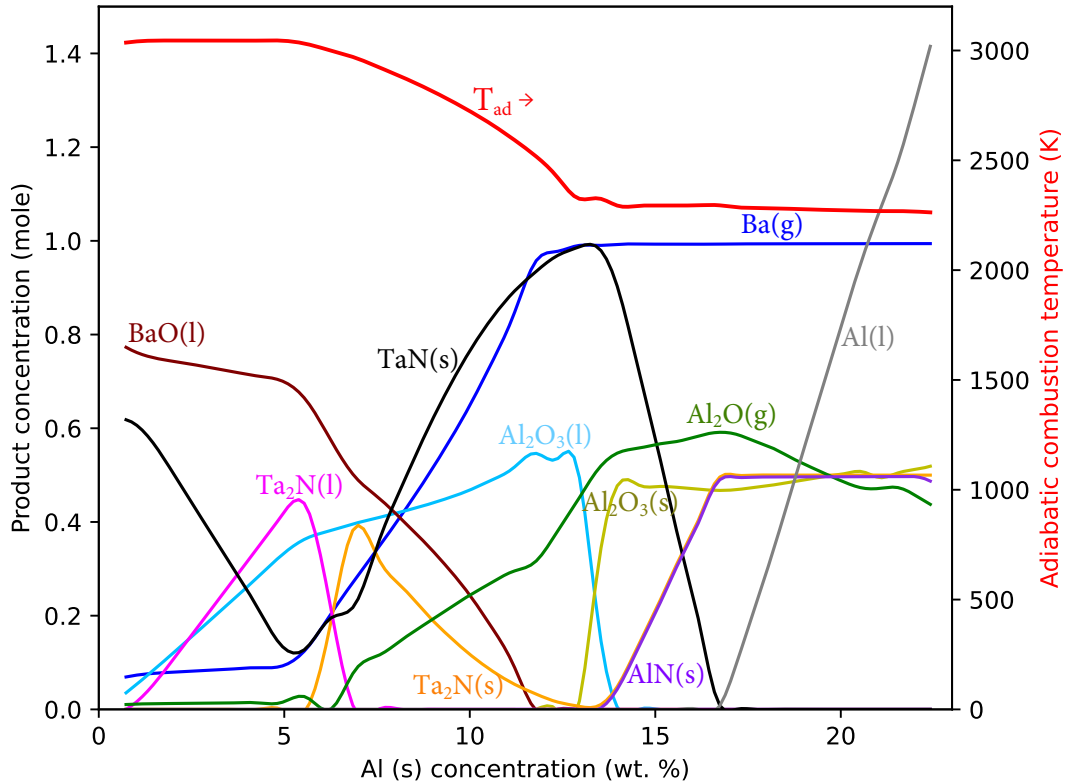


Figure 5.6: Adiabatic combustion temperature and equilibrium concentration of reaction products by varying the fuel to oxidizer ratio for Al/BaTaO<sub>2</sub>N.

Figure 5.6 shows dependence of adiabatic combustion temperature and equilibrium concentration of reaction products on the fuel to oxidizer ratio for Al/BaTaO<sub>2</sub>N system. This system showed maximum adiabatic combustion temperature of value 3045 K with 4.93 wt.% of the fuel which then starts decreasing uniformly until  $\approx$  2300 K corresponding to 13 wt.% of the fuel and then remains constant throughout further variation of fuel. Compounds like BaO, Ta<sub>2</sub>N, Al<sub>2</sub>O<sub>3</sub> as well as Al showed liquid phase while some product compounds like Ta<sub>2</sub>N, Al<sub>2</sub>O<sub>3</sub>, AlN and TaN was observed to be in solid phases. Ba and Al<sub>2</sub>O are the only gas phase generated throughout the

variation of reactants stoichiometry. Both Ba (g) and Al<sub>2</sub>O (g) appeared from the start of the variation. Ba (g) increased sharply beyond 5 wt.% of fuel reaches the maximum of 1 mole with 12 wt.% and remained constant afterwards. In case the Al<sub>2</sub>O (g) the value starts appearing slowly which then starts increasing as the fuel concentration increases, reaching the maximum value of 0.6 moles and then decreases.

The perovskite type of oxynitrides showed a consistent result for the adiabatic combustion temperature which was typically above 3000 K with maximum value of 3187 K for CaTaO<sub>2</sub>N corresponding to 7.5 wt.% of aluminum fuel and minimum of 3045 K for BaTaO<sub>2</sub>N corresponding to 4.93 wt.% of aluminum.

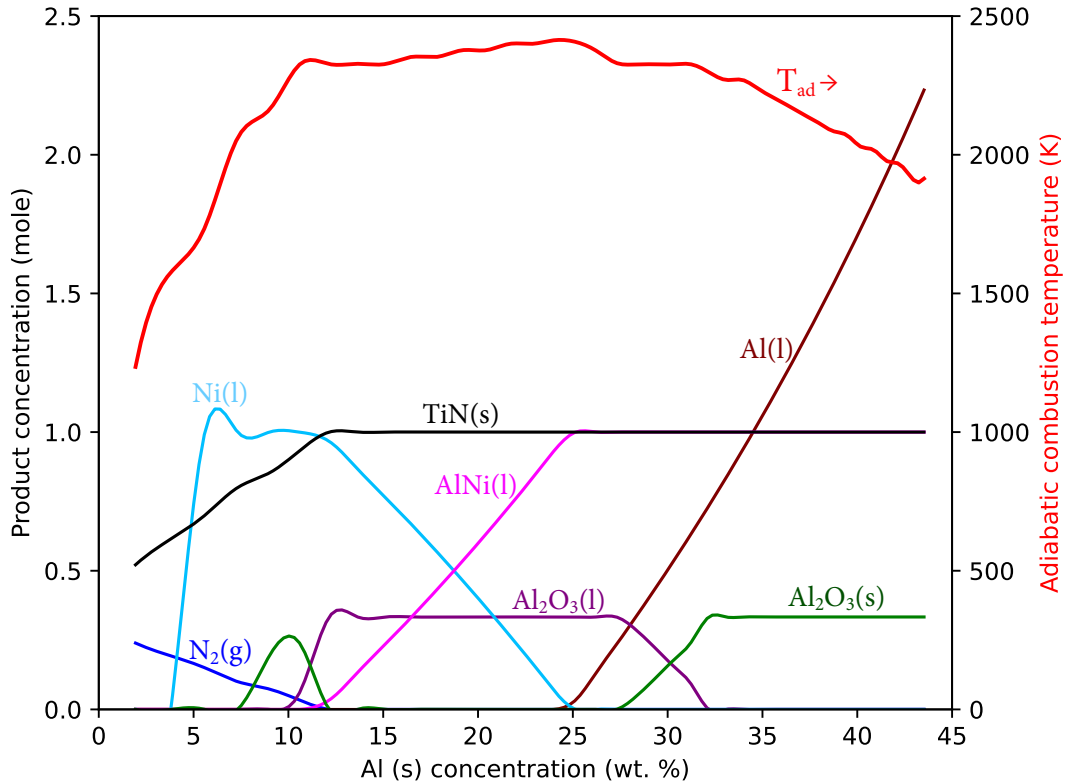


Figure 5.7: Adiabatic combustion temperature and equilibrium concentration of reaction products by varying the fuel to oxidizer ratio for Al/TiNiON system.

Figure 5.7 shows dependence of adiabatic combustion temperature and equilibrium concentration of reaction products on the fuel to oxidizer ratio for Al/TiNiON system. The calculation revealed lower combustion temperature compared to perovskite oxynitrides but still high

with maximum value of 2413 K for 24.02 wt.% of fuel. In case of perovskite oxynitride the temperature seemed very high from the beginning whereas in TiNiON, it showed less in the beginning and goes on increasing sharply until 11 wt.% of the fuel concentration. Since, titanium has very high melting point it remained in the solid state, combining with nitrogen, forming titanium nitride (TiN) throughout the different stoichiometry whose concentration remained constant of 1 mole after 12 wt.% of aluminum fuel. Aluminum nickel and aluminum in liquid phase showed linearly increasing trend starting from 11 wt.% and 25 wt.% of fuel respectively. Nitrogen (N<sub>2</sub>) is the only gas phase appeared in the beginning and disappeared after increasing aluminum concentration beyond 12 wt.%. Oxides of aluminum showed liquid state corresponding to high combustion temperature which switched to solid form as the temperature goes decreasing.

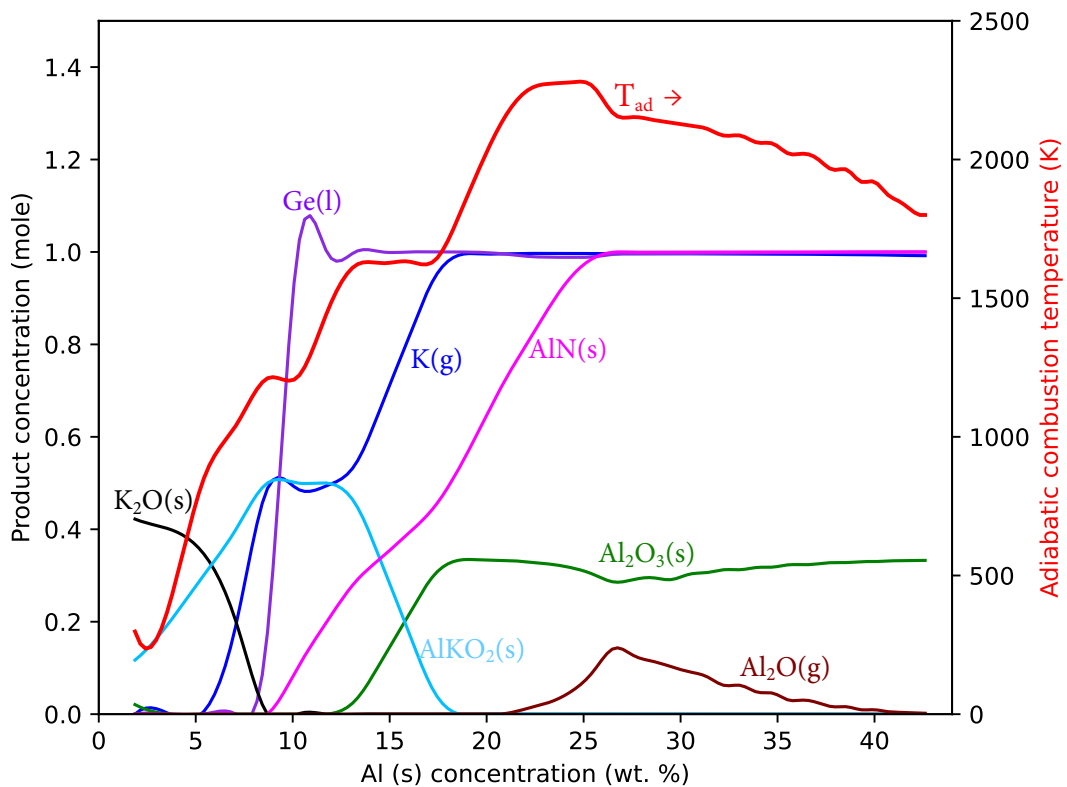


Figure 5.8: Adiabatic combustion temperature and equilibrium concentration of reaction products by varying the fuel to oxidizer ratio for Al/KGeON system.

Figure 5.8 shows dependence of adiabatic combustion temperature and equilibrium concentration of reaction products on the fuel to oxidizer ratio for Al/KGeON system. The maxi-

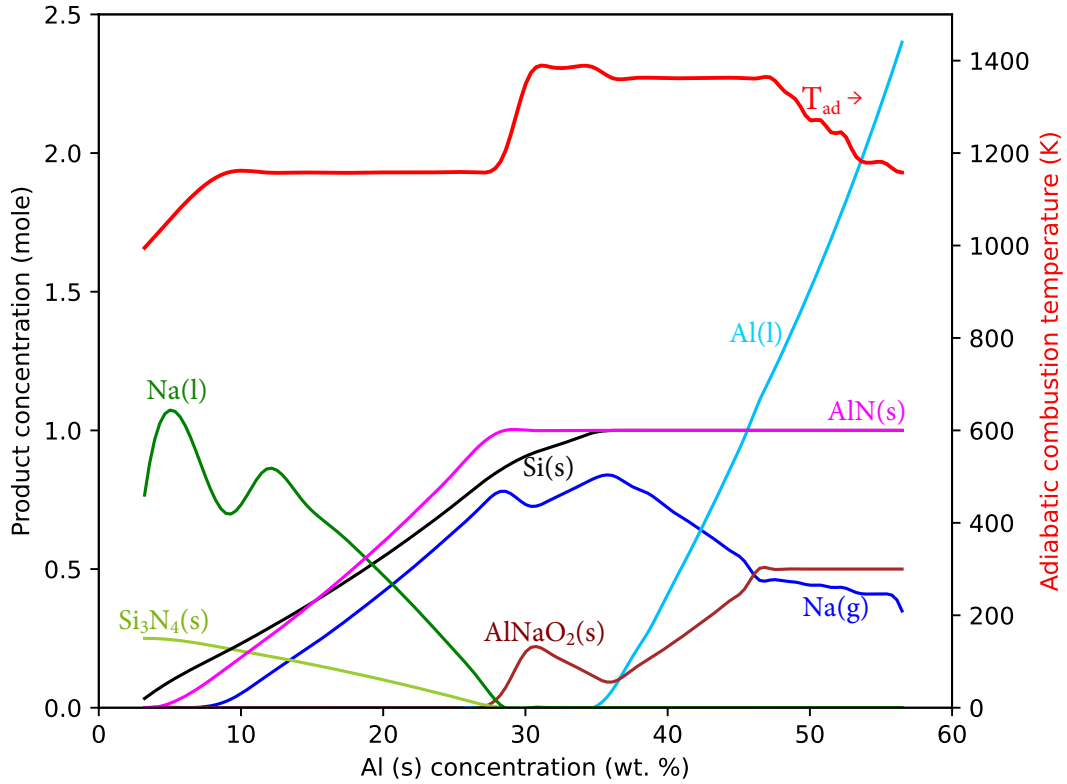


Figure 5.9: adiabatic combustion temperature and equilibrium concentration of reaction products by varying the fuel to oxidizer ratio for Al/NaSiON system.

imum adiabatic combustion temperature reached the value 2279 K corresponding to 24.45 wt.% of aluminum and most of the equilibrium products appeared in solid phase including  $K_2O$ ,  $AlKO_2$ , AlN, and  $Al_2O_3$ . Germanium (Ge) is the only liquid phase appeared from around 9 wt.% of aluminum with temperature over 1200 K and remained constant of 1 mole throughout the tuned stoichiometry. The gas phase of potassium (K) also appeared after 5 wt.% of the fuel and goes on increasing and remained constant with 1 mole concentration. In addition, fuel concentration above 20 wt.% also gave the aluminum oxide,  $Al_2O$  in gas phase.

Figure 5.9 shows dependence of adiabatic combustion temperature and equilibrium concentration of reaction products on the fuel to oxidizer ratio for Al/NaSiON system. The system showed the lowest maximum combustion temperature among all the formulations with value 1386 K for 34.74 wt.% of fuel. The major products include solid phases such as silicon (Si), aluminum nitride (AlN), silicon nitride ( $Si_3N_4$ ) and  $AlNaO_2$ . Sodium in liquid phase starts appear-

ing from the beginning, fluctuates sometimes and terminates to zero corresponding to 29 wt.% of fuel. Moreover, aluminum liquid appeared from 35 wt.% of aluminum and increased sharply to reach nearly 1.5 moles of aluminum liquid with 50 wt.% of fuel. Sodium is the only gas phase to contribute for the gas generation.

### 5.1.2 Volumetric and Gravimetric Energy Release out of the Exothermic Reactions

Energy is the most important factor for a nano-energetic system for its performance during detonation and for its various applications. In the gas phase of the equilibrium products, a high Pressure  $\times$  Volume (PV) value also refers high energy. Figure 5.10 shows the volumetric

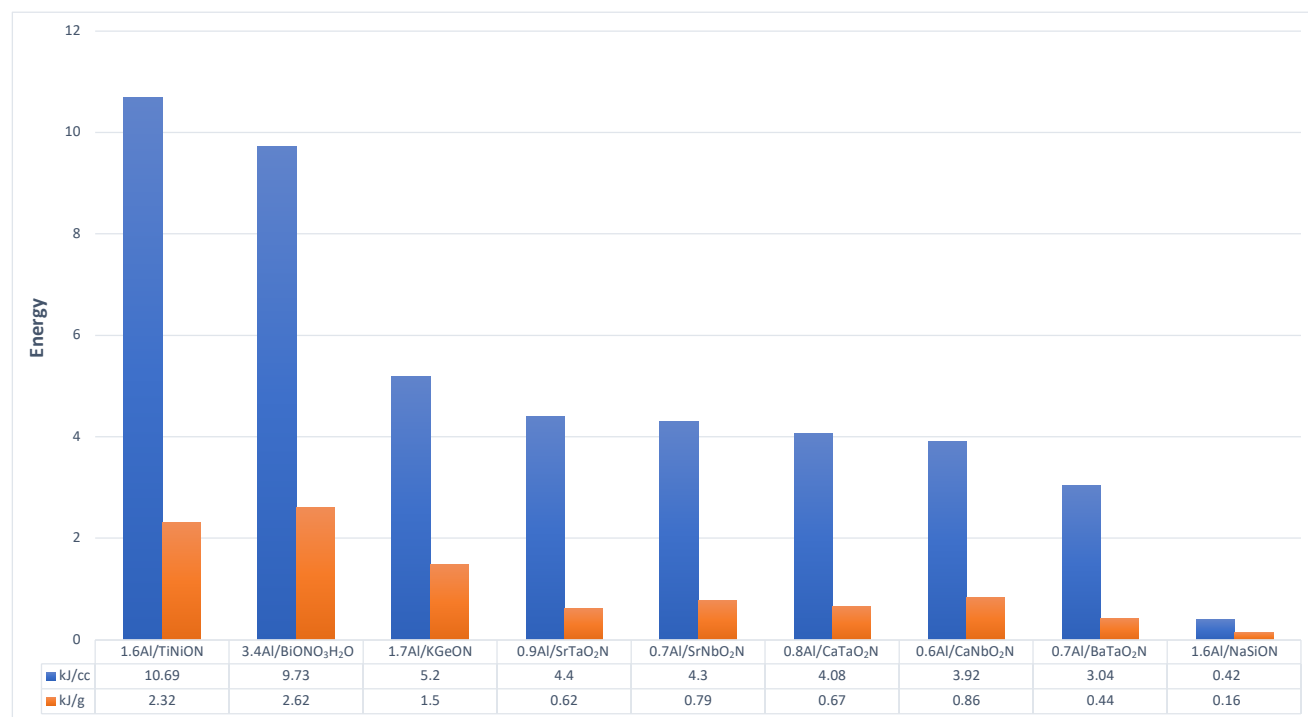


Figure 5.10: Volumetric and gravimetric energy release for the most favorable stoichiometry of Al-oxynitride formulation.

energy (per unit volume) and gravimetric energy (per unit mass) release out of the nine chosen aluminum-metal oxynitride formulations corresponding to peak combustion temperature with their stoichiometry are shown in Figure 5.10. As the energy can neither be created nor be destroyed, it can only be transferred from one form to another and so, from such nano-energetics the chemical energy stored in the compounds are released in the form of several other forms of

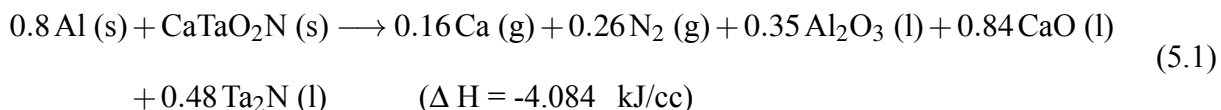
energy. Depending upon the situation to use, both volumetric and gravimetric energy release needs to be understood.

Out of all chosen formulations, Al/TiNiON showed the maximum value of volumetric energy release with value 10.699 kJ/cc corresponding to 1.6Al/TiNiON stoichiometry of the reactants which is followed by Al/BiONO<sub>3</sub>·H<sub>2</sub>O composites with value -9.730 kJ/cc corresponding to 23.12 wt.% of aluminum fuel. All perovskite type of oxynitrides showed uniform energy generation of above 4.00 kJ/cc with 7 to 8 wt.% of fuel except BaTaO<sub>2</sub>N for which the energy generation was only 3.043 kJ/cc with 4.93 wt.% of fuel. Moreover, NaSiON showed less energy release of only 0.423 kJ/cc corresponding to 34.74 wt.% of fuel whereas, KGeON showed a decent value of volumetric energy release with value 5.2 kJ/cc corresponding to 1.7Al/KGeON stoichiometry.

### 5.1.3 Reactions Involved of Favorable Reactant's Stoichiometry

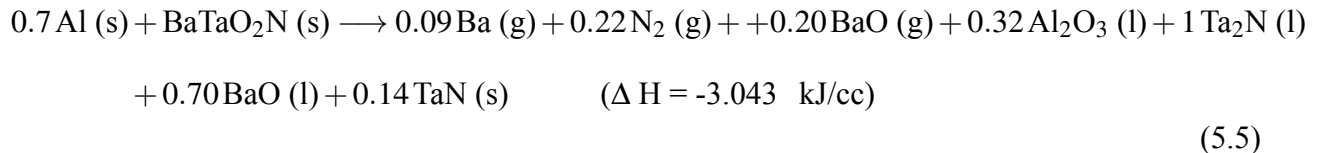
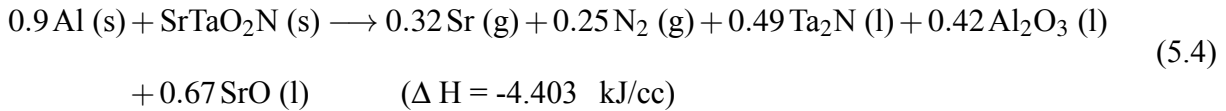
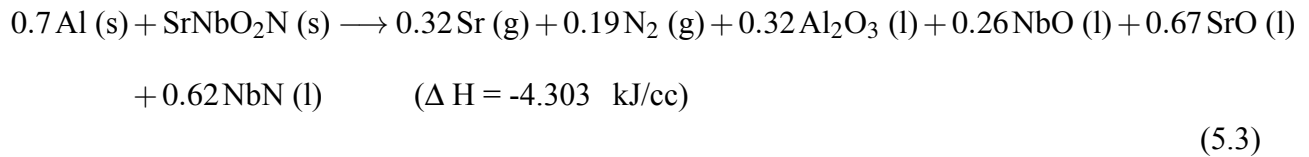
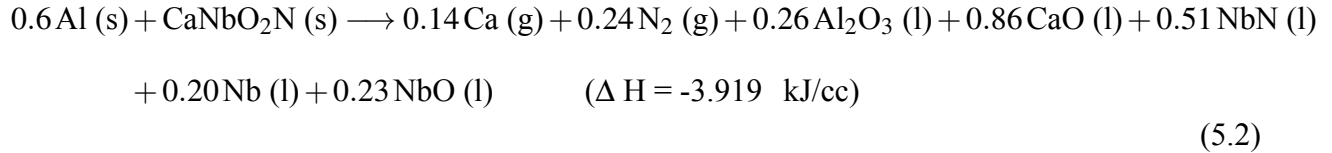
The reaction was carried out keeping the concentration of oxidizer fixed to one mole and varying the concentration of fuel to reach the stoichiometry with best detonation, energy release and gas discharge performance. The nano-energetics are characterized by their exothermic chemical reaction of reactants where the energy is release during the combustion. Here the suitable choice of reactants proportion was taken for the one which generates the maximum adiabatic combustion temperature with extreme severity of the reaction.

For CaTaO<sub>2</sub>N, 0.8 mole of aluminum generated the peak adiabatic combustion temperature with 0.35Al<sub>2</sub>O<sub>3</sub> (l), 0.84CaO (l) and 0.48Ta<sub>2</sub>N (l) as the major equilibrium products along with some gas phases of Al, Ca, N<sub>2</sub> and Al<sub>2</sub>O. The reaction involved is shown below.

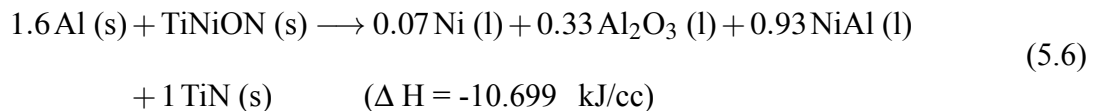


Similar reaction scenarios were obtained for other perovskite oxynitrides ABO<sub>2</sub>N (A = Ba, Sr, Ca and, B = Nb, Ta) where the huge amount of gas release was mainly due to the forma-

tion of gas phase of alkaline earth metals (Ba, Sr, and Ca) and the aluminum oxides at extremely high combustion temperature.

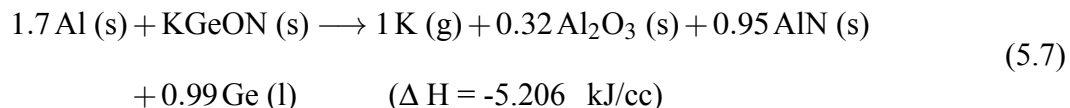


TiNiON showed no gas generation even with peak combustion temperature of 2413 K. Nickel (Ni), nickel aluminum (NiAl) and aluminum oxide (Al<sub>2</sub>O<sub>3</sub>) appeared in liquid state as shown in the reaction below.

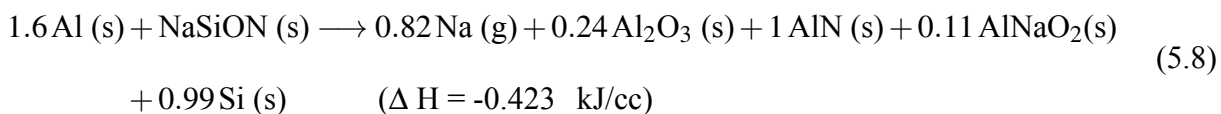


KGeON, on the other hand, showed five different gas phases with aluminum (Al), germanium (Ge), potassium (K), aluminum oxide (Al<sub>2</sub>O) and nitrogen (N<sub>2</sub>). However, some forms of

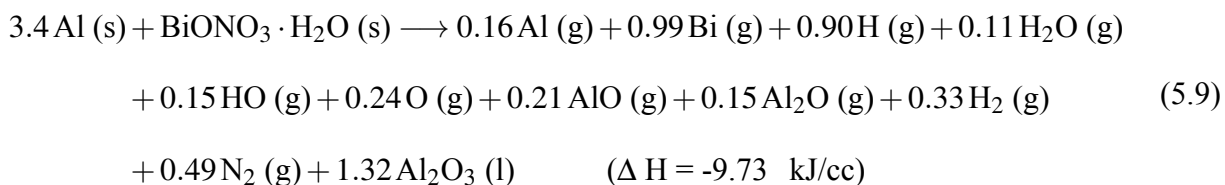
aluminum like aluminum nitride (AlN) and oxides of aluminum remained in solid state as shown below.



For NaSiON, with low peak temperature of 1386 K, only sodium occurred as gas phase and other products such as silicon (Si), aluminum nitride (AlN), aluminum sodium oxide (AlNaO<sub>2</sub>) and aluminum oxide appeared in solid phases as shown below.



Similarly, for BiONO<sub>3</sub>·H<sub>2</sub>O the peak adiabatic combustion temperature of 3639 K was observed for 23.12 wt.% of fuel. The equilibrium composition of products observed are in gas phase with bismuth, hydrogen and nitrogen being the major gas products. In addition, the significant amount of aluminum oxide was appeared in liquid phase as shown in reaction below.



#### 5.1.4 Amount of Gas Release out of the Exothermic Reaction of Reactant Mixtures

Gas discharge is another important factor to consider for several applications including propellant and biocidal treatment. During detonation, high combustion temperature turns the solid phases of reactants to liquid and then liquid to gas phase. The gas discharge behavior of nano energetic materials during combustion plays an important role in understanding and opti-

mizing their performance, especially in the propulsion systems, making it a critical area of study in the field of energetic materials. Nano energetic materials, characterized by their nanoscale dimensions and enhanced reactivity, exhibit unique combustion characteristics compared to their bulk counterparts. Prediction of gas discharge during a highly exothermic reaction provides valuable insights into the combustion kinetics, temperature profiles, and gas-phase reaction products. Additionally, studying gas discharge aids in assessing safety aspects, as it contributes to the understanding of potential hazardous by-products and emissions. It is important to characterize the gas-phase composition and dynamics to refine the formulation of nano energetic materials for the applications ranging from propulsion systems to pyrotechnics.

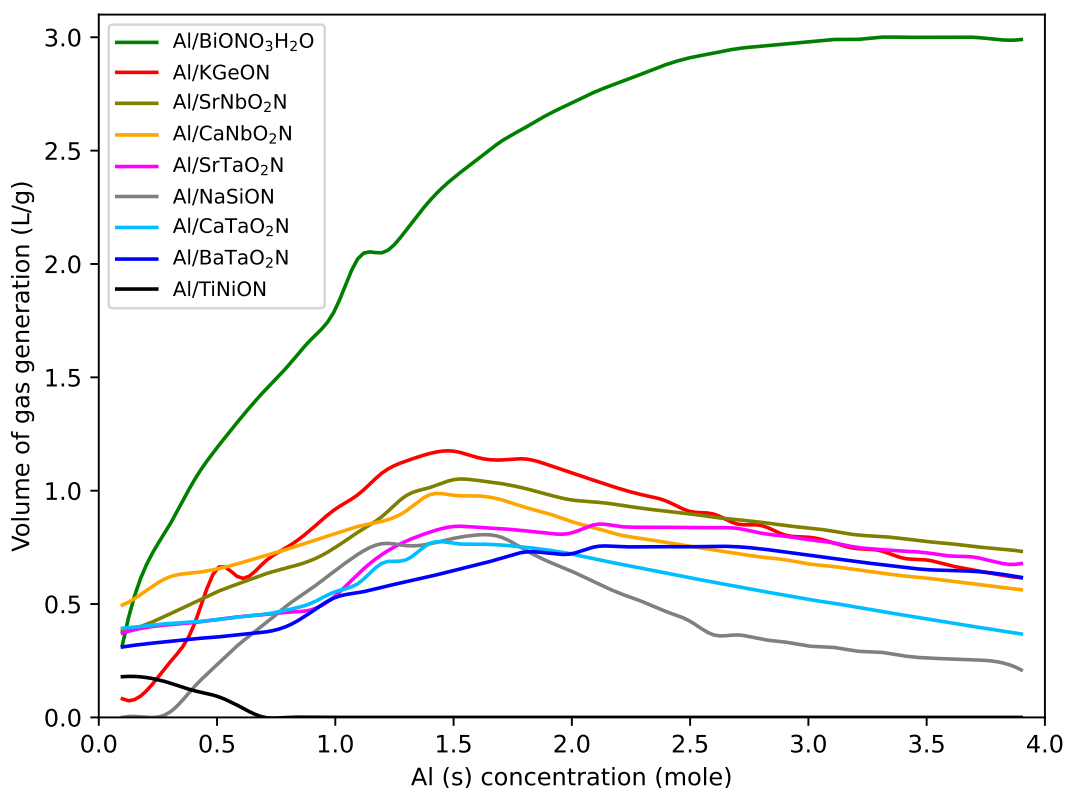


Figure 5.11: Variation of gas generation for different metal oxynitride formulations by varying fuel to oxidizer ratio.

Figure 5.11 summarizes all gas phase releases in liter/gm of reactants and concentrations of fuel used. All of the gases products initially starts increasing with increasing concentration of the fuel and hence the generated temperature. The increment lasts until the combustion tem-

perature starts decreasing beyond a certain proportion of the fuel and then starts decreasing. For metal perovskite oxynitride, the volume of gas released corresponding to peak adiabatic combustion temperature ranged from 0.376 L/g for Al/BaTaO<sub>2</sub>N to 0.681 L/g for Al/CaNbO<sub>2</sub>N with 4.93 wt.% of aluminum and 8.29 wt.% of aluminum, respectively.

Table 5.1: Thermite reactants and their corresponding gas species.

<b>Thermite reactants</b>	<b>Product gas species</b>
0.8 Al (s) + CaTaO <sub>2</sub> N (s)	0.16 Ca, 0.26 N <sub>2</sub>
0.6 Al (s) + CaNbO <sub>2</sub> N (s)	0.14 Ca, 0.24 N <sub>2</sub>
0.7 Al (s) + SrNbO <sub>2</sub> N (s)	0.32 Sr, 0.19 N <sub>2</sub>
0.9 Al (s) + SrTaO <sub>2</sub> N (s)	0.32 Sr, 0.25 N <sub>2</sub>
0.7 Al (s) + BaTaO <sub>2</sub> N (s)	0.09 Ba, 0.22 N <sub>2</sub> , 0.20 BaO
1.6 Al (s) + TiNiON (s)	–
1.7 Al (s) + KGeON (s)	1 K
1.6 Al (s) + NaSiON (s)	0.82 Na
3.4 Al (s) + BiONO <sub>3</sub> ·H <sub>2</sub> O (s)	0.16 Al, 0.99 Bi, 0.9 H, 0.11 H <sub>2</sub> O, 0.15 HO, 0.24 O, 0.21 AlO, 0.15 Al <sub>2</sub> O, 0.33 H <sub>2</sub> , 0.49 N <sub>2</sub>

Table 5.1 shows the reactant's stoichiometry for the favorable reaction and their corresponding gases species generated. For all the perovskite oxynitrides the volume of gas is mainly due to the gases phase of alkaline earth metals (Barium, Strontium and Calcium) and oxides of aluminum as well as nitrogen. Interestingly, Al/TiNiON, showed no gas generation corresponding to peak combustion temperature of 2413 K whereas Al/BiONO<sub>3</sub>·H<sub>2</sub>O reaction results in several different forms of gases species and hence become the highest gas releasing composites among all chosen systems with value more than 3 liter/g of the reactant mixtures.

In terms of volume of gas generation, TiNiON followed BiONO<sub>3</sub>·H<sub>2</sub>O with value of 1.135 L/g with 24.45 wt.% of fuel. However, the maximum amount of gas discharge value can be different than the value corresponding to peak adiabatic combustion temperature. With all the oxidizers taken except TiNiON, the volume of gas generation showed first increasing with increasing concentration of fuel, reached the maximum value and then decreases with further increase in the concentration of fuel.

Table 5.2: Maximum adiabatic combustion temperature, gas generation and energy release for several oxidizer compounds.

Oxidizer	Fuel, Al(s)	$T_{ad}(\text{max})$ (K)	$V_{gas}$ (L/g)	Energy release	
				(kJ/cc)	(kJ/g)
BiONO <sub>3</sub> ·H <sub>2</sub> O	23.12%	3639	3.004	-9.730	-2.620
CaTaO <sub>2</sub> N	7.48%	3187	0.475	-4.084	-0.665
CaNbO <sub>2</sub> N	8.29%	3165	0.681	-3.919	-0.863
SrNbO <sub>2</sub> N	7.70%	3078	0.632	-4.303	-0.789
SrTaO <sub>2</sub> N	7.17%	3058	0.475	-4.403	-0.624
BaTaO <sub>2</sub> N	4.93%	3045	0.376	-3.043	-0.437
TiNiON	24.02%	2413	0	-10.699	-2.104
KGeON	24.45%	2279	1.135	-5.206	-1.506
NaSiON	34.74%	1386	0.805	-0.423	-0.157

The overall scenario of the expected thermodynamic and energy parameters is summarized in Table above (Table 5.2). It was seen that the perovskite metal oxynitrides showed uniform characteristic for combustion temperature, gas discharge volumes and energy release. Among, all the oxynitrides taken, BiONO<sub>3</sub>·H<sub>2</sub>O came with the maximum combustion temperature of value 3639 K which is way greater than any other chosen metal oxynitrides. The extremely high combustion temperature over 3000 K, favored for high gas discharge and high energy release in majority of the chosen systems. Al/TiNiON and Al/KGeON also showed a high temperature well above 2000 K but earlier generates no gas discharge at all while the later generates a high value of gas discharge among all chosen formulations with value 1.135 L/g. In addition, NaSiON showed a very low amount of energy release 0.805 kJ/cc with a decent value of gas discharge.

## 5.2 Density Functional Theory (DFT) Analysis

### 5.2.1 Electronic Band Structure and Density of States (DOS)

The electronic band structure of materials significantly affects their nanoenergetic properties, which include their reaction behavior at the nanoscale, such as combustion, detonation, and energy and gas release. While examining electronic structure of a system, the band gap is very crucial which refers to the energy difference between the top of the valence band, also called valence band maximum (VBM) and the bottom of the conduction band, also called conduction band

minimum (CBM). The nature of this band gap can be either direct or indirect, depending on the momentum (k-vector) of the electrons. If both the VBM and CBM are located corresponding to the same wave vector then it gives a direct band gap whereas if they correspond to two different wave vector then the band gap thus calculated is called indirect band gap. Also, the Density of States (DOS) is a fundamental concept in solid-state physics that describes the number of electronic states available within a given energy range in a material. It's crucial for understanding various electronic properties of materials, including conductivity, optical properties, and thermal properties.

High reactivity in nanoenergetic materials often requires a high DOS near the Fermi level, ensuring a sufficient number of accessible electronic states for rapid reactions. Efficient charge transfer, facilitated by a suitable band structure, further enhances this reactivity. The ease of initiating a reaction, or ignition sensitivity, is influenced by the band gap and the DOS; materials with smaller band gaps and higher DOS at the Fermi level are more easily ignited due to better electronic conductivity and more available states for reaction initiation. The energy release rate in nanoenergetic reactions is tied to the mobility of charge carriers and the availability of electronic states, with a lower effective mass (indicating higher mobility) and a higher DOS enabling faster energy release. While materials with larger band gaps tend to be more thermally stable, they are generally less reactive. Therefore, optimizing the band structure to balance stability and reactivity is crucial for designing effective nanoenergetic materials. Moreover, the band gap determines the wavelengths of light that can be absorbed by the nanoenergetic material. This is crucial for applications like photothermal conversion, where absorbed light is converted to heat for reaction ignition by light source.

- Perovskite type of oxynitrides ( $ABO_2N$ ): Figure 5.12 shows  $CaTaO_2N$  has a direct band gap with a value of 1.1932 eV indicating the compound as a semiconductor with a small band gap. The energy levels of the VBM and CBM are 4.2834 eV and 5.4766 eV, respectively, while the Fermi energy is positioned at 4.8219 eV. Also, the DOS diagram is in good agreement with the band structure diagram where the DOS value is high in the re-

gions corresponding to complex interactions shown in band diagram. For energetic materials, high conductivity is not essential, but the ability to undergo rapid electronic transitions can be beneficial. The small band gap of 1.1932 eV in  $\text{CaTaO}_2\text{N}$  allows for these rapid transitions as electrons can easily be excited from the valence band to the conduction band, contributing to the material's reactivity. The position of the Fermi energy close to the CBM

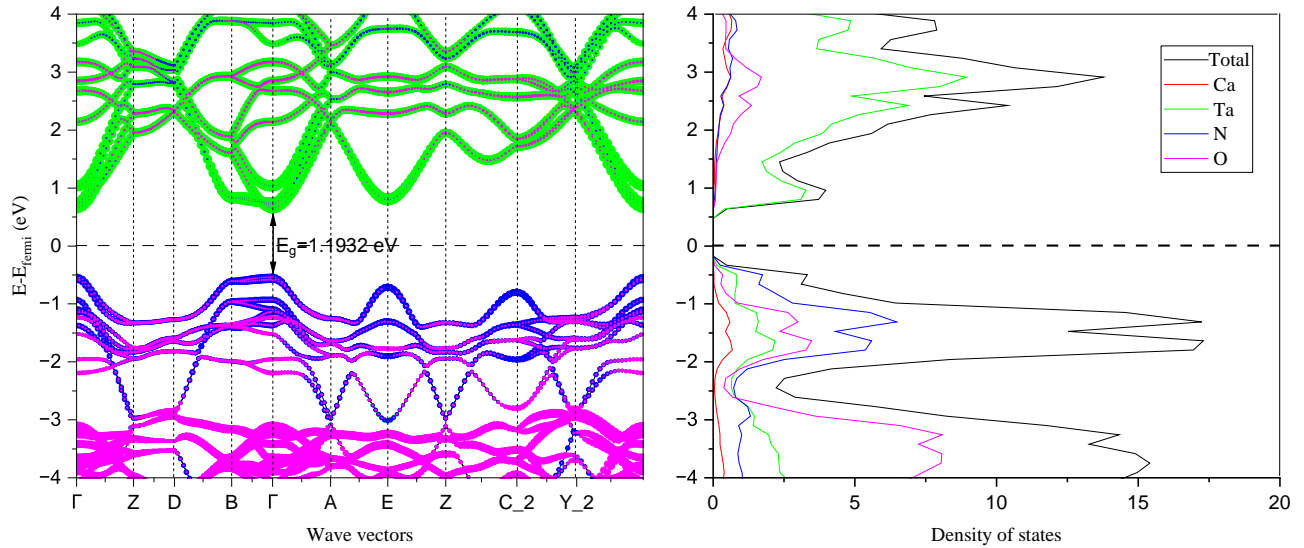


Figure 5.12: Electronic band structure and density of states of  $\text{CaTaO}_2\text{N}$ .

suggests that electrons can be readily excited to the conduction band, enhancing the reactivity of  $\text{CaTaO}_2\text{N}$  as an oxidizer. The DOS diagram indicating high DOS near the VBM and CBM implies that there are many available states for electron transitions, supporting rapid electronic transitions.

- Potassium germanium oxynitride ( $\text{KGeON}$ ): Figure 5.13 shows electronic band structure and density of states of  $\text{KGeON}$ .  $\text{KGeON}$  exhibits an indirect band gap semiconductor character with a band gap of 2.5060 eV, where the valence band maximum (VBM) is at 1.2539 eV and the conduction band minimum (CBM) at 3.7598 eV. This indirect band gap suggests that electron transitions involve a change in momentum, typically requiring assistance from phonons. The Fermi energy of 1.7976 eV indicates the material's intrinsic semiconductor behavior, positioned between the VBM and CBM. As an energetic material,

KGeON may face challenges due to its indirect band gap, which can limit the efficiency of energy absorption and release compared to direct band gap semiconductors. This characteristic could hinder its suitability for applications requiring rapid and efficient energy release, such as in explosive materials or fast-reacting pyrotechnics.

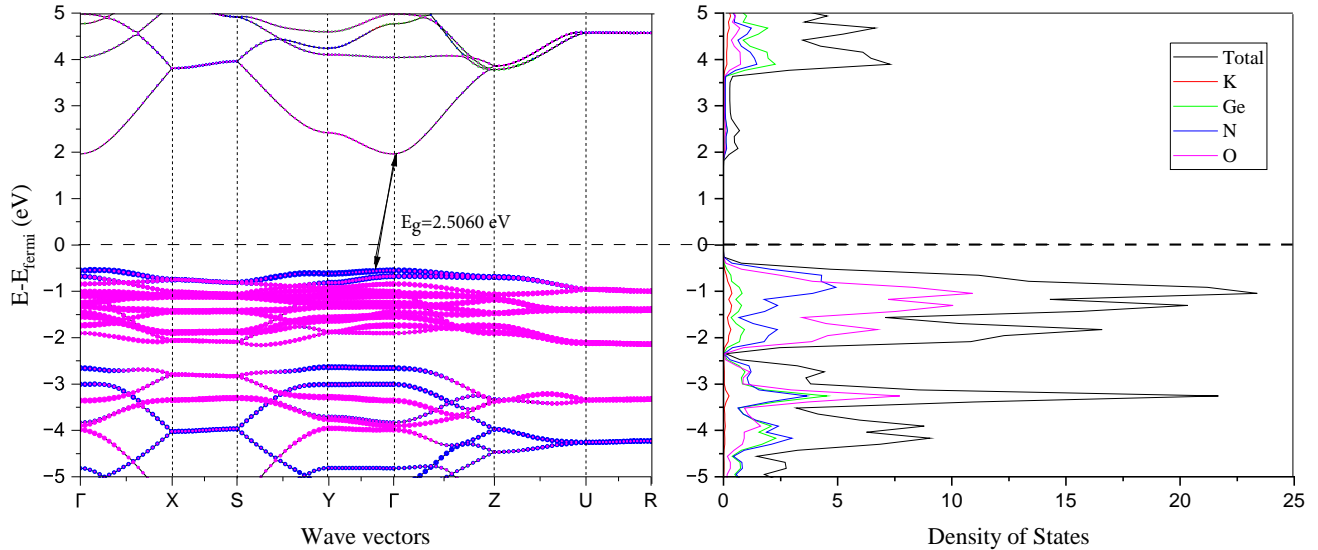


Figure 5.13: Electronic band structure and density of states of KGeON.

- Sodium silicon oxynitride (NaSiON): Figure 5.14 shows electronic band structure and density of states of NaSiON. NaSiON is characterized by an indirect band gap of 1.5157 eV. This band structure indicates that electron transitions between the valence band maximum (VBM) at 5.4812 eV and the conduction band minimum (CBM) at 6.9969 eV require a change in momentum, often facilitated by phonons. The Fermi energy of 5.9507 eV places it between the VBM and CBM, consistent with its semiconductor nature. Comparatively, KGeON also features an indirect band gap but with a larger band gap of 2.5060 eV, where its VBM and CBM are situated at 1.2539 eV and 3.7598 eV, respectively. Both materials share similarities in their indirect band gap nature and Fermi energy positioning and are not showing a good insight for potential nano-energetic material.

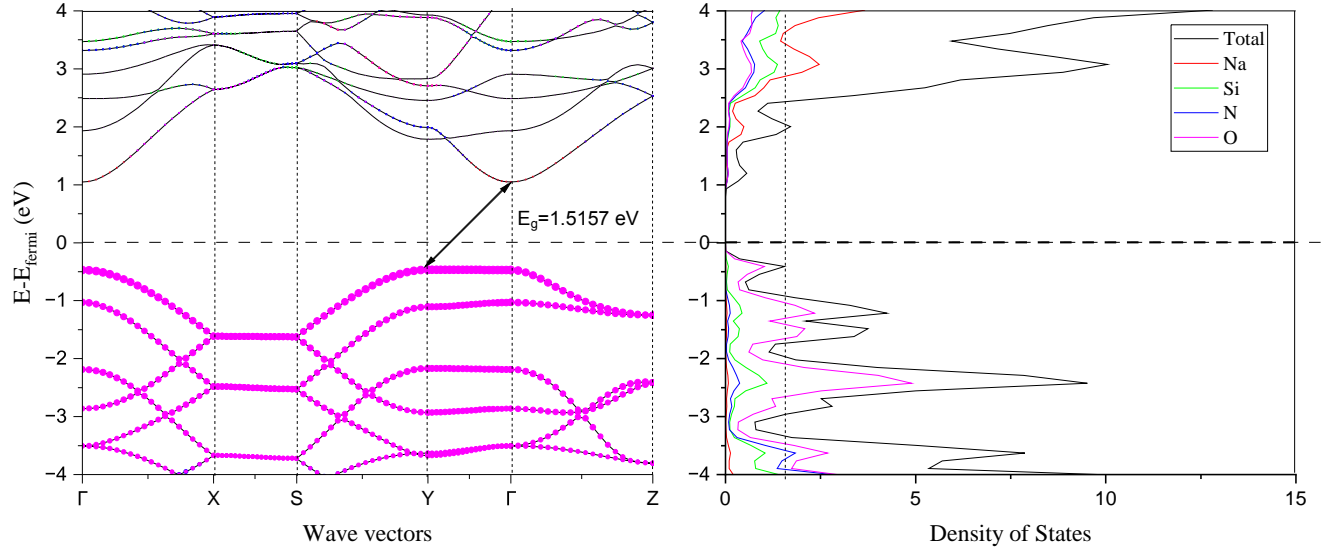


Figure 5.14: Electronic band structure and density of states of NaSiON.

### 5.2.2 Optical Properties Calculations

For a compound to act effectively as an oxidizer in an energetic system, its optical properties play a crucial role. The absorption spectrum should be selective, allowing the compound to absorb light at specific wavelengths corresponding to the energy required for initiating chemical reactions. A high absorption coefficient at these wavelengths ensures that the compound can absorb sufficient light energy to start the reaction process. The absorption coefficient  $\alpha$ , which typically has units of  $\text{cm}^{-1}$ , quantifies how much light of a specific wavelength is absorbed per unit distance as it travels through a material. The formula for the absorption coefficient is derived from the complex refractive index and the dielectric function of the material.

The absorption coefficient  $\alpha$  can be expressed as:

$$\alpha = \frac{4\pi k}{\lambda} \quad (5.10)$$

where:  $k$  is the extinction coefficient (the imaginary part of the complex refractive index) and  $\lambda$  is the wavelength of the light in centimeters.

Additionally, the refractive index can influence how light interacts with the compound,

affecting the propagation and focusing of light within the material, while the dielectric constant (both real and imaginary parts) indicates the material's ability to absorb and convert light energy into chemical energy. The refractive index of a material is a fundamental optical property that indicates how light propagates through the material. It is defined as the ratio of the speed of light in a vacuum to the speed of light in the material:

$$n = \frac{\text{speed of light in vacuum } (c)}{\text{speed of light in medium/material } (v)} \quad (5.11)$$

A higher refractive index means the material is optically denser, causing light to slow down more and bend more sharply at the interface between the two mediums. While dealing with the optical property, the dielectric constant (or relative permittivity) of a material is a complex quantity that describes how an electric field interacts with the material. It is crucial in understanding the optical properties of a compound, particularly how it absorbs and refracts light.

The dielectric constant,  $\epsilon(\omega)$ , is typically expressed as a complex function:

$$\epsilon(\omega) = \epsilon'(\omega) + i\epsilon''(\omega) \quad (5.12)$$

Where,

- $\omega$  is the angular frequency of the electric field (or light).
- $\epsilon'(\omega)$  is the real part of the dielectric constant.
- $\epsilon''(\omega)$  is the imaginary part of the dielectric constant.

The real part of the dielectric constant,  $\epsilon'(\omega)$ , represents the material's ability to store electrical energy. It is associated with the refractive index  $n(\omega)$  of the material and describes how light propagates through the material without being absorbed.

$$\epsilon'(\omega) = n^2(\omega) - k^2(\omega) \quad (5.13)$$

Where,  $n(\omega)$  is the refractive index.

The imaginary part of the dielectric constant,  $\epsilon''(\omega)$ , represents the material's ability to absorb electrical energy.

$$\epsilon''(\omega) = 2n(\omega)k(\omega) \quad (5.14)$$

It is associated with the loss of energy from the electromagnetic wave as it propagates through the material and is closely related to the absorption coefficient  $\alpha(\omega)$ .

Sensitivity to light is a critical factor for oxidizers to avoid accidental ignition while ensuring reliable intentional ignition. For accidental ignition prevention, the compound should not be overly sensitive to ambient light, and its absorption peaks should ideally lie outside the range of typical environmental light exposure. Thermal stability under normal light conditions is essential to prevent unintended decomposition. For intentional ignition, the compound should have strong absorption peaks at specific wavelengths that match the energy of the applied light source, ensuring efficient energy conversion to initiate the desired reaction.

- Perovskite type of oxynitrides: Figure 5.15 shows optical properties of CaTaO<sub>2</sub>N illustrating its behavior in terms of absorption, refractive index, and dielectric constant across a range of photon energies. The oxidizer was investigated as a representative compound for perovskite type of oxynitride as well as being the one with highest combustion temperature generation and energy release. The Figure 5.15(a) displays the absorption coefficient (in cm<sup>-1</sup>) as a function of photon energy (eV) for different crystallographic directions (XX, YY, ZZ). There are distinct peaks in the absorption spectrum for each direction, suggesting anisotropy in the absorption properties of CaTaO<sub>2</sub>N. The material absorbs light differently along different crystallographic axes. The onset of significant absorption occurs from around 1.2 eV, which aligns well with the band gap energy ( $\approx 1.1932$  eV) previously discussed, indicating electronic transitions near the band edge. The peak absorption throughout the range of photon energy is obtained at  $\approx 11$  eV with corresponding wavelength of 113 nm for all crystallographic directions with the value  $\approx 1.55 \times 10^6$  cm<sup>-1</sup>.

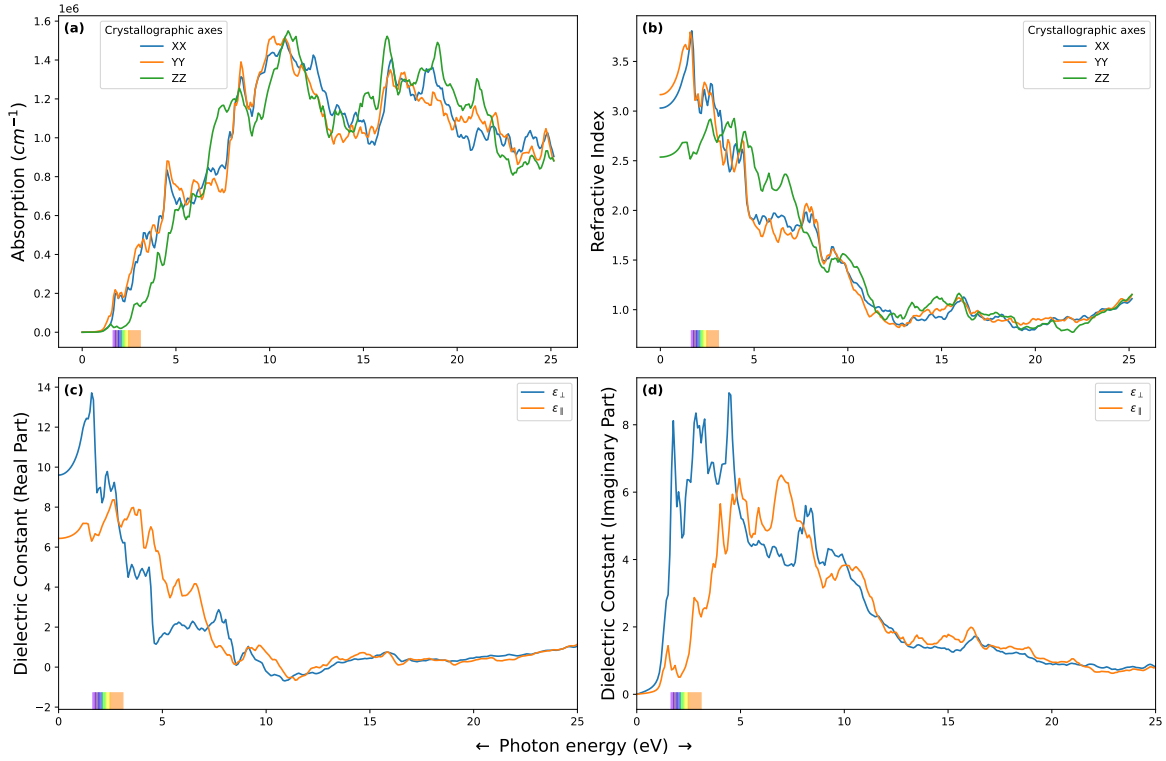


Figure 5.15: Optical properties of  $\text{CaTaO}_2\text{N}$ .

The second plot, Figure 5.15(b), shows the variation of refractive index with the photon energy. There is a noticeable dispersion in the refractive index at lower energies specifically corresponding to the visible range and below, which stabilizes at higher energies. At different photon energies, the electric field of the light interacts differently with the electrons in the material. When the photon energy is close to the electronic transition energies of the material (i.e., near the band gap), the electrons can be more easily polarized, resulting in a higher refractive index.

The Figure 5.15(c) and (d) shows the behavior of dielectric constant of the material with photon energy in two perpendicular crystallographic axes. The dielectric constant, comprising both real and imaginary parts, is fundamentally linked to a material's optical properties through its influence on the refractive index and light absorption. From the figure shown, both the real and imaginary part of the dielectric constant reveals the anisotropic nature of the material. The value of dielectric constant for real part varies significantly with the crys-

tal axis which starts from 9.5 and 6.5 for perpendicular and parallel axes respectively. The values showed maximum in the visible range and then decreased with several fluctuations until for nearly 11 eV and then remains constant. On the other hand, the imaginary part has a significant difference in perpendicular and parallel component values up until 5 eV. The perpendicular component reaches a maximum value of 9 whereas parallel reaches to 6.5 corresponding to energy nearly 5 eV.

- Potassium germanium oxynitride (KGeON): Figure 5.16 shows optical properties of KGeON. The KGeON starts absorbing the photon with energy just above the visible region which reaches its maximum peak of  $1.3 \times 10^6 \text{ cm}^{-1}$  at 11 eV photon with a corresponding wavelength of 113 nm and then decrease slowly beyond. The materials refractive index for visible rays is around 2 which shows little increase in the value as energy increases and decreases uniformly until 12.5 eV photon energy.

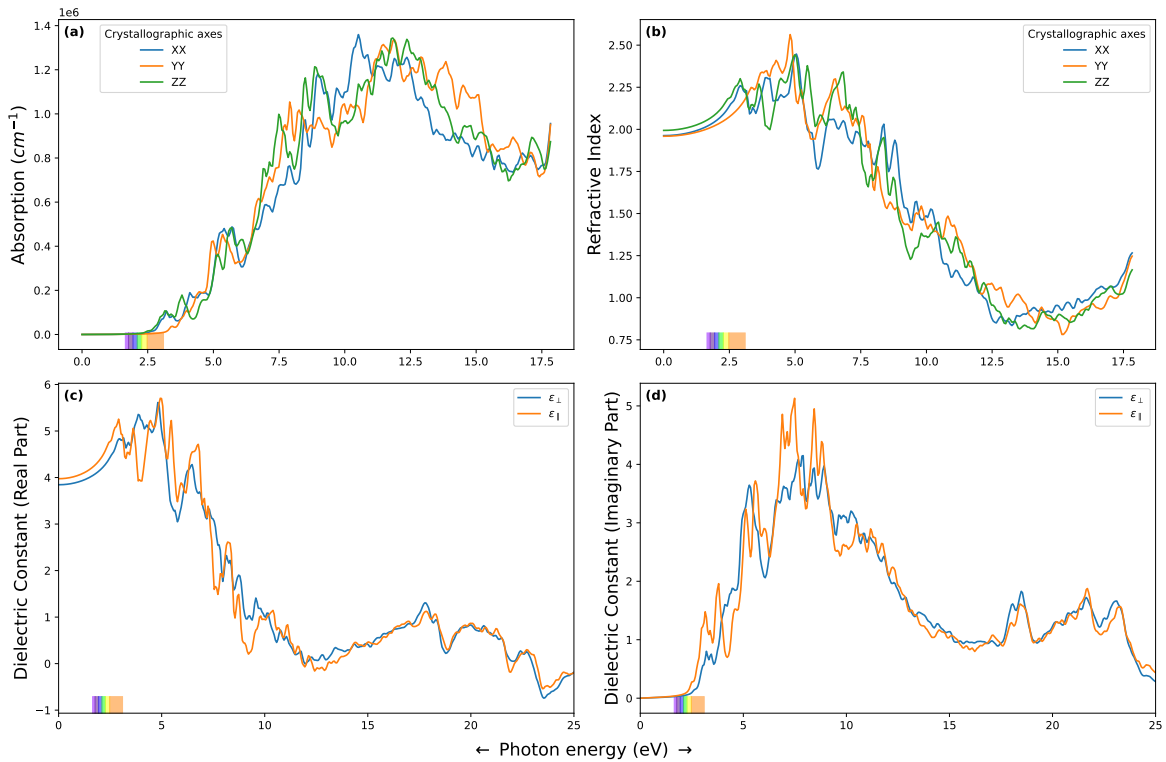


Figure 5.16: Optical properties of KGeON.

The dielectric constant for real part showed its maximum at value 5.5 corresponding to 5 eV photon and decreases to zero and then fluctuates beyond, whereas imaginary part showed its maximum at 5 for parallel interaction corresponding to 7.5 eV photon and then decreases and fluctuates beyond.

- Sodium silicon oxynitride (NaSiON): Comparing with NaSiON, (shown in Figure 5.17), the absorption is very low for visible radiations which starts increasing with maximum value of just above  $1.75 \times 10^6 \text{ cm}^{-1}$  at 15 eV of photon energy with corresponding wavelength of 82.66 nm. The refractive index values showed a highest peak value along YY axis of just greater than 3. The value starts decreasing as the energy increases. The values of real part of dielectric constant ranges between 3 to 6 in and around the visible region with peak value of 6.5 for perpendicular interaction then decreases as the energy increases. In case of imaginary part the peak dielectric constant was obtained at 6.7 corresponding to 6 eV of photon energy.

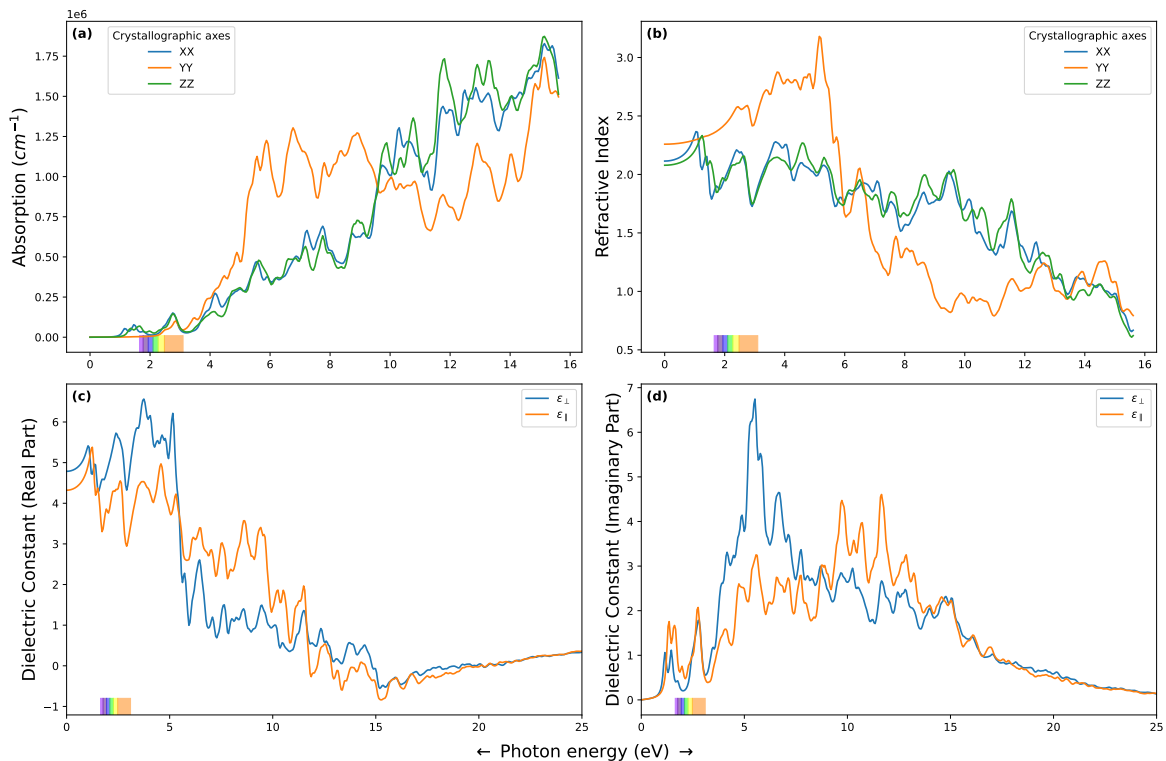


Figure 5.17: Optical properties of NaSiON.

## CHAPTER VI

### CONCLUSIONS

This comprehensive investigation has illuminated the potential of Al-metal oxynitride composites as a potential nanoenergetic material, showcasing remarkable attributes crucial for diverse applications. The study revealed that these composites exhibit an impressive energy release, surpassing established values found in the literature for the most well-known combinations of metal oxides and hydroxides with aluminum. Notably, the combustion temperature soared to over 3600 K for  $\text{BiONO}_3 \cdot \text{H}_2\text{O}$ , underscoring the superiority of Al-metal oxynitride composites in terms of thermal performance. Moreover, the gas generation capabilities were striking, particularly evident in the Al/ $\text{BiONO}_3 \cdot \text{H}_2\text{O}$  composite which demonstrated a volumetric gas generation of value 3.004 L/g corresponding to 23.12 wt.% of fuel, followed by the Al/KGeON composite with value 1.135 L/g corresponding to 24.45 wt.% of fuel. The magnitude of gas pressure discharge is a critical parameter for propulsion systems, making these findings particularly relevant for advancements in propulsion technology. In addition,  $\text{BiONO}_3 \cdot \text{H}_2\text{O}$  emerged as the frontrunner as energetic materials, showcasing the high value of energy release of -9.730 kJ/cc, corresponding to an unparalleled combustion temperature of 3639 K. These results underscore the promising potential of Al-metal oxynitride composites, not only for their elevated combustion temperature but also for their substantial gas generation capabilities, positioning them as highly potential energetic composites in the class of advanced energetic materials.

Perovskite type of oxynitride showed consistent result for temperature, energy release and volume of gas generation. Among perovskite type,  $\text{CaTaO}_2\text{N}$ , with 7.48 wt.% of fuel showed the maximum combustion temperature of 3187 K followed by  $\text{CaNbO}_2\text{N}$  with value 3165 K. The energy released out of exothermic reaction of perovskite oxynitride were observed from -3.043

kJ/cc for BaTaO<sub>2</sub>N corresponding to 4.93 wt.% of fuel to -4.403 kJ/cc for SrTaO<sub>2</sub>N corresponding to 7.17 wt.% of fuel.

Furthermore, the result from Al/TiNiON with high energy release of -10.699 kJ/cc and high combustion temperature of 2413 K but no gas generation seemed interesting and may come with some application in situations where no gas generation is desired but needs greater energy and temperature, in metal welding, for instance. The high energy release in the Al/TiNiON system is primarily due to the highly exothermic formation of titanium nitride (TiN) and aluminum oxide (Al<sub>2</sub>O<sub>3</sub>). Titanium remains solid during the reaction, efficiently forming TiN with nitrogen, a process that releases significant heat. Additionally, aluminum reacts vigorously with both oxygen and nitrogen in TiNiON, further contributing to the energy output. The system achieves an optimal fuel-to-oxidizer ratio around 11 wt.% aluminum, maximizing exothermic reactions and resulting in a sharp increase in combustion temperature up to 2413 K. The absence of significant gas generation beyond 12 wt.% aluminum ensures that most of the energy remains within the reaction medium, enhancing the overall energy density and efficiency of the system. KGeON also showed decent values of combustion temperature, gas, and energy release with values 2279 K, 1.135 L/g and -5.206 kJ/cc respectively.

The first principal computational DFT study also supports the high combustion and high energy release of Al/CaTaO<sub>2</sub>N oxynitride. The small and direct band gap of 1.1932 eV suggest the rapid electronic transitions between the valence band and conduction band thereby resulting in extreme high temperature and energy release. The proximity of the Fermi energy to the CBM suggests that electrons can be easily excited to the conduction band, which enhances the reactivity of CaTaO<sub>2</sub>N as an oxidizer. Additionally, the high DOS near the VBM and CBM indicates many available states for electron transitions, facilitating rapid electronic transitions. On the other hand, the optical properties of CaTaO<sub>2</sub>N exhibit significant anisotropy, with distinct absorption peaks along different crystallographic axes and notable dispersion in the refractive index at lower photon energies. The onset of significant absorption aligns with the band gap energy, indicating effective electronic transitions near the band edge. This sensitivity to light, particularly

in the visible range, makes CaTaO<sub>2</sub>N a promising candidate for light-initiated reactions in energetic materials. The ability to efficiently absorb and interact with light facilitates rapid electronic transitions, enhancing the reactivity of CaTaO<sub>2</sub>N as an oxidizer and offering potential for tailored initiation methods based on crystallographic orientation. KGeON, despite its indirect band gap of 2.5060 eV, which typically suggests less efficient energy absorption and release due to the need for phonon assistance in electron transitions, demonstrated high energy and gas release. This indicates that other factors, such as the material's chemical composition and structural properties, contribute significantly to its energetic performance. The intrinsic semiconductor behavior, as evidenced by the Fermi energy positioned between the VBM and CBM, might still support sufficient electronic transitions to facilitate effective energy and gas release, making KGeON a viable candidate for applications requiring high energy output. Moreover, regarding optical properties, it is noted that the material begins absorbing photons just above the visible region, with peak absorption occurring at 11 eV, where the absorption coefficient reaches  $1.3 \times 10^6 \text{ cm}^{-1}$ . This indicates that KGeON efficiently interacts with photons of this energy, suggesting a strong sensitivity to light. NaSiON is unsuitable for energetic materials due to its indirect band gap of 1.5157 eV, which requires phonon assistance for electron transitions between the VBM at 5.4812 eV and the CBM at 6.9969 eV. Additionally, it shows minimal absorption of visible radiation and modest optical properties, including low absorption coefficients and refractive index values, indicating limited potential for efficient light interaction and reaction initiation in energetic applications.

The aluminum-metal oxynitride composite selected for examination has demonstrated highly promising characteristics, showcasing its exceptional capacity to generate extremely high temperatures and release significant energy. These notable findings position the chosen composites winning over well-established traditional monomolecular explosives such as TNT and RDX. In the contemporary scientific landscape, where nano energetic composites have gathered a substantial attention for their diverse applications, the conducted thermodynamic analysis on oxynitrides assumes great importance. This analysis contributes valuable insights into the latent potential of metal oxynitrides as energetic materials, presenting a nuanced understanding of their

performance. The investigated oxynitrides have shown considerable promise across major properties, encompassing energy release, gas generation, and combustion temperature. However, a thorough comprehension of their sensitivity, stability, and efficiency in specific applications necessitates further in-depth exploration. It is worth noting that the predominant focus of current nano energetics research revolves around metal oxides and hydroxides, with a notable absence of dedicated studies on oxynitride compounds. Thus, the undertaken thermodynamic analysis stands as a pioneering initiative, marking a crucial step in elucidating the thermodynamic feasibility of oxynitrides in the field of nano energetics. This exploration not only addresses an existing gap in the literature but also lays the groundwork for future investigations and advancements in this emerging area of research. The versatility inherent in oxynitrides opens a spectrum of potential applications based on their distinctive properties. Compositions capable of generating extreme temperatures and thermal pulses present themselves as viable explosives in domains such as mining and construction, where controlled energy release is important. Simultaneously, those demonstrating high values of gas discharge assume significance in propulsion systems and pyrotechnics, promising advancements in these technological realms. The pursuit of oxynitrides as energetic materials not only diversifies the landscape of nanoenergetic research but also holds the promise of transformative applications across a variety of sectors, fueling further interest and exploration in this field.

## REFERENCES

- [1] Tonio Andrade. *The gunpowder age: China, military innovation, and the rise of the West in world history*. Princeton University Press, 2017.
- [2] Jack Kelly. *Gunpowder: alchemy, bombards, and pyrotechnics: the history of the explosive that changed the world*. Basic Books (AZ), 2004.
- [3] Paul Redner. The history, chemistry, and physics of energetic materials. *Energetic Materials: Thermophysical Properties, Predictions, and Experimental Measurements*, page 7, 2010.
- [4] Kevin J Anderson. Energetic materials, part ii: Tnt and other military explosives. *MRS Bulletin*, 14(12):63–64, 1989.
- [5] Hugh DC Smyth. Propellant-driven metered-dose inhalers for pulmonary drug delivery. *Expert opinion on drug delivery*, 2(1):53–74, 2005.
- [6] DD Dlott. Thinking big (and small) about energetic materials. *Materials science and technology*, 22(4):463–473, 2006.
- [7] Karen S Martirosyan, Leizheng Wang, Arol Vicent, and Dan Luss. Nanoenergetic gas-generators: Design and performance. *Propellants, Explosives, Pyrotechnics: An International Journal Dealing with Scientific and Technological Aspects of Energetic Materials*, 34(6):532–538, 2009.
- [8] Karen S Martirosyan, L Wang, and D Luss. Novel nanoenergetic system based on iodine pentoxide. *Chemical Physics Letters*, 483(1-3):107–110, 2009.
- [9] KS Martirosyan, L Wang, A Vicent, and D Luss. Synthesis and performance of bismuth trioxide nanoparticles for high energy gas generator use. *Nanotechnology*, 20(40):405609, 2009.
- [10] Karen S Martirosyan. Nanoenergetic gas-generators: principles and applications. *Journal of Materials Chemistry*, 21(26):9400–9405, 2011.
- [11] Karen S Martirosyan, Maxim Zyskin, Charles M Jenkins, et al. Modeling and simulation of pressure waves generated by nano-thermite reactions. *Journal of Applied Physics*, 112(9), 2012.
- [12] Karen S Martirosyan and Maxim Zyskin. Reactive self-heating model of aluminum spherical nanoparticles. *Applied Physics Letters*, 102(5), 2013.

- [13] Karen S Martirosyan, Maxim Zyskin, Charles M Jenkins, et al. Fluid dynamic modeling of nano-thermite reactions. *Journal of Applied Physics*, 115(10), 2014.
- [14] Karen S Martirosyan. High-density nanoenergetic gas generators. In *Handbook of Nanoscience, Engineering, and Technology*, pages 762–781. CRC Press, 2012.
- [15] Ziru Liu. Review and prospect of thermal analysis technology applied to study thermal properties of energetic materials. *FirePhysChem*, 1(3):129–138, 2021.
- [16] Srбуhi A Yolchinyan, Ryker W Eads, Mkhitar A Hobosyan, and Karen S Martirosyan. Hydroxide-based nanoenergetic materials. *Propellants, Explosives, Pyrotechnics*, 44(4):464–471, 2019.
- [17] Thomas M Klapötke. Energetic materials encyclopedia. In *Energetic Materials Encyclopedia*. de Gruyter, 2018.
- [18] Mohamed Gaber Zaky, Ahmed Elbeih, and Tamer Elshenawy. Review of nano-thermites: A pathway to enhanced energetic materials. *Central European Journal of Energetic Materials*, 18(1), 2021.
- [19] Mkhitar Hobosyan, Sergey E Lyshevski, and Karen S Martirosyan. Integrated micropropulsion systems with nanoenergetic propellants. In *Nanomaterials in Rocket Propulsion Systems*, pages 403–420. Elsevier, 2019.
- [20] V Eric Sanders, Blaine W Asay, Timothy J Foley, Bryce C Tappan, Adam N Pacheco, and Steven F Son. Reaction propagation of four nanoscale energetic composites (al/moo<sub>3</sub>, al/wo<sub>3</sub>, al/cuo, and b12o<sub>3</sub>). *Journal of Propulsion and Power*, 23(4):707–714, 2007.
- [21] Srбуhi A Yolchinyan, Mkhitar A Hobosyan, and Karen S Martirosyan. Tailoring bismuth oxide flower-, bowtie-and brushwood-like structures through microfluidic synthesis. *Materials Chemistry and Physics*, 207:330–336, 2018.
- [22] Mkhitar A Hobosyan, Srбуhi A Yolchinyan, and Karen S Martirosyan. A novel nano-energetic system based on bismuth hydroxide. *RSC advances*, 6(71):66564–66570, 2016.
- [23] MR Weismiller, JY Malchi, JG Lee, RA Yetter, and TJ Foley. Effects of fuel and oxidizer particle dimensions on the propagation of aluminum containing thermites. *Proceedings of the Combustion Institute*, 33(2):1989–1996, 2011.
- [24] Carole Rossi. Two decades of research on nano-energetic materials. *Propellants, Explosives, Pyrotechnics*, 39(3):323–327, 2014.
- [25] Karen S. Martirosyan. Concise encyclopedia of self-propagating high-temperature synthesis, in 1st edition: History, theory, technology, and products. In *Concise Encyclopedia of Self-Propagating High-Temperature Synthesis*, pages 208–209. Elsevier, 2017.
- [26] Ng Hsiao Yen and Lee Yiew Wang. Reactive metals in explosives. *Propellants, Explosives, Pyrotechnics*, 37(2):143–155, 2012.

- [27] Weiqiang Pang, Xuezhong Fan, Ke Wang, Yimin Chao, Huixiang Xu, Zhao Qin, and Fengqi Zhao. Al-based nano-sized composite energetic materials (nano-cems): Preparation, characterization, and performance. *Nanomaterials*, 10(6):1039, 2020.
- [28] Dilip Sundaram, Vigor Yang, and Richard A Yetter. Metal-based nanoenergetic materials: synthesis, properties, and applications. *Progress in Energy and Combustion Science*, 61:293–365, 2017.
- [29] Karen S. Martirosyan. Concise encyclopedia of self-propagating high-temperature synthesis, in 1st edition: History, theory, technology, and products. In *Concise Encyclopedia of Self-Propagating High-Temperature Synthesis*, pages 206–207. Elsevier, 2017.
- [30] Vladimir E Zarko. The prospects of using nanoenergetic materials in solid rocket propulsion. In *Nanomaterials in Rocket Propulsion Systems*, pages 3–30. Elsevier, 2019.
- [31] Vladimir E Zarko. Nanoenergetic materials: a new era in combustion and propulsion. In *Energetic nanomaterials*, pages 1–20. Elsevier, 2016.
- [32] Mkhitar A Hobosyan and Karen S Martirosyan. Novel nanoenergetic materials: emerging trends and applications. *IEEE Nanotechnology Magazine*, 14(1):30–36, 2019.
- [33] Mkhitar A Hobosyan and Karen S Martirosyan. Tuning the reactivity of nano-energetic gas generators based on bismuth and iodine oxidizers. *Nano-Energetic Materials*, pages 191–212, 2019.
- [34] M. Hobosyan, A. Kazansky, and K.S. Martirosyan. Nanoenergetic composite based on  $I_2O_5/Al$  for biological agent defeat. *Nanotech*, 3:599–602, 2012.
- [35] Kyle T Sullivan, Chunwei Wu, Nicholas W Piekielek, Karen Gaskell, and Michael R Zachariah. Synthesis and reactivity of nano- $Ag_2O$  as an oxidizer for energetic systems yielding antimicrobial products. *Combustion and Flame*, 160(2):438–446, 2013.
- [36] Ivan Davila. *Biocidal Defeat Agents Produced by Silver-Iodine Nanoenergetic Gas Generators*. The University of Texas Rio Grande Valley, 2017.
- [37] Carole Rossi, Kaili Zhang, Daniel Esteve, Pierre Alphonse, Philippe Tailhades, and Constantin Vahlas. Nanoenergetic materials for mems: a review. *Journal of Microelectromechanical Systems*, 16(4):919–931, 2007.
- [38] Karen S Martirosyan and Sergey E Lyshevski. Memes technology microthrusters and nanoenergetic materials for micropropulsion systems. In *2012 2nd International Conference "Methods and Systems of Navigation and Motion Control" (MSNMC)*, pages 133–136. IEEE, 2012.
- [39] Karen S Martirosyan, M Hobosyan, and Sergey E Lyshevski. Enabling nanoenergetic materials with integrated microelectronics and mems platforms. In *2012 2nd International Conference "Methods and Systems of Navigation and Motion Control" (MSNMC)*, pages 999–1003. IEEE, 2012.

- [40] Alexandro Trevino, Mkhitar A Hobosyan, Ivan Davila, Karen S Martirosyan, and Sergey E Lyshevski. Design and characterization of thermoplastic microthrusters with nanothermite intermolecular composites. In *2020 IEEE 40th International Conference on Electronics and Nanotechnology (ELNANO)*, pages 662–666. IEEE, 2020.
- [41] Ivan Puchades, Lynn F Fuller, Sergey E Lyshevski, Mkhitar Hobosyan, Liu Ting, and Karen S Martirosyan. Mems and 3d-printing microthrusters technology integrated with hydroxide-based nanoenergetic propellants. In *2017 IEEE 37th International Conference on Electronics and Nanotechnology (ELNANO)*, pages 67–70. IEEE, 2017.
- [42] Svatopluk Zeman and Marcela Jungová. Sensitivity and performance of energetic materials. *Propellants, Explosives, Pyrotechnics*, 41(3):426–451, 2016.
- [43] Xue-Xue Zhang, Zhi-Jian Yang, Fude Nie, and Qi-Long Yan. Recent advances on the crystallization engineering of energetic materials. *Energetic Materials Frontiers*, 1(3-4):141–156, 2020.
- [44] Richard A Yetter. Progress towards nanoengineered energetic materials. *Proceedings of the Combustion Institute*, 38(1):57–81, 2021.
- [45] Luigi T DeLuca. Overview of al-based nanoenergetic ingredients for solid rocket propulsion. *Defence Technology*, 14(5):357–365, 2018.
- [46] MR Weismiller, JY Malchi, RA Yetter, and TJ Foley. Dependence of flame propagation on pressure and pressurizing gas for an al/cuo nanoscale thermite. *Proceedings of the Combustion Institute*, 32(2):1895–1903, 2009.
- [47] Amparo Fuertes. Synthetic approaches in oxynitride chemistry. *Progress in Solid State Chemistry*, 51:63–70, 2018.
- [48] Stefan G Ebbinghaus, Hans-Peter Abicht, Richard Dronskowski, Thomas Müller, Armin Reller, and Anke Weidenkaff. Perovskite-related oxynitrides—recent developments in synthesis, characterisation and investigations of physical properties. *Progress in Solid State Chemistry*, 37(2-3):173–205, 2009.
- [49] Anita Rachel, Stefan G Ebbinghaus, Martin Güngerich, Peter J Klar, Jan Hanss, Anke Weidenkaff, and Armin Reller. Tantalum and niobium perovskite oxynitrides: synthesis and analysis of the thermal behaviour. *Thermochimica Acta*, 438(1-2):134–143, 2005.
- [50] Franck Tessier, Pascal Maillard, François Cheviré, Kazunari Domen, and Shinichi Kikkawa. Optical properties of oxynitride powders. *Journal of the Ceramic Society of Japan*, 117(1361):1–5, 2009.
- [51] Manan Ahmed and Guo Xinxin. A review of metal oxynitrides for photocatalysis. *Inorganic Chemistry Frontiers*, 3(5):578–590, 2016.
- [52] Young-Il Kim, Patrick M Woodward, Karim Z Baba-Kishi, and Cheuk W Tai. Characterization of the structural, optical, and dielectric properties of oxynitride perovskites  $am_2n$  ( $a = ba, sr, ca$ ;  $m = ta, nb$ ). *Chemistry of materials*, 16(7):1267–1276, 2004.

- [53] Anit Joseph and Tiju Thomas. Recent advances and prospects of metal oxynitrides for supercapacitor. *Progress in Solid State Chemistry*, page 100381, 2022.
- [54] A Shiryaev. Thermodynamics of shs processes: An advanced approach. *International Journal of Self Propagating High Temperature Synthesis*, 4:351–362, 1995.
- [55] William R Smith. Hsc chemistry for windows, 2.0. *Journal of Chemical Information and Computer Sciences*, 36(1):151–152, 1996.
- [56] Holger Wolff and Richard Dronskowski. First-principles and molecular-dynamics study of structure and bonding in perovskite-type oxynitrides  $ABO_2N$  (A= Ca, Sr, Ba; B= Ta, Nb). *Journal of computational chemistry*, 29(13):2260–2267, 2008.
- [57] Nathaniel E Brese and Michael O’Keeffe. Crystal chemistry of inorganic nitrides. *Complexes, clusters and crystal chemistry*, pages 307–378, 2005.
- [58] J Guyader, R Jacquet, JM Malhaire, G Roullet, and Y Laurent. Préparation et structure de kgeon: un composé à liaison potassium-azote. *Revue de chimie minérale*, 20(6):863–870, 1983.
- [59] David S Sholl and Janice A Steckel. *Density functional theory: a practical introduction*. John Wiley & Sons, 2022.

## VITA

Manoj Chhetri originates from Nepal, a country rich in cultural heritage and natural beauty. He holds a Master of Science (M.S.) degree in Physics from Tribhuvan University, Nepal, earned in 2018. Mr. Chhetri furthered his academic pursuits by completing a second Master of Science (M.S.) degree in Interdisciplinary Studies from The University of Texas Rio Grande Valley (UTRGV) in August 2024.

During his time at UTRGV, Mr. Chhetri was honored with the prestigious Dean's Graduate Assistantship (DGA) and engaged in research focused on computational nano-energetic materials. His higher academic journey began with a Bachelor of Science (B.S.) in Physics, also attained from Tribhuvan University. Looking ahead, Mr. Chhetri aspires to continue his academic journey in Physics, driven by his passion for scientific inquiry and innovation.

**Manoj Chhetri**

Email: [chhetrimanoj1992@gmail.com](mailto:chhetrimanoj1992@gmail.com)